Particuology xxx (xxxx) xxx

Contents lists available at ScienceDirect

Particuology

journal homepage: www.elsevier.com/locate/partic

X-ray imaging techniques for gas–solid fluidized beds: A technical review

Matteo Errigo, Paola Lettieri, Massimiliano Materazzi*

Department of Chemical Engineering, University College London, Gower St, London, United Kingdom

ARTICLE INFO

Article history:
Received 6 September 2023
Received in revised form
24 October 2023
Accepted 16 November 2023
Available online xxx

Keywords:
X-ray digital radiography
X-ray computed tomography
X-ray imaging techniques
Gas solid fluidized bed

ABSTRACT

Gas–solid fluidized beds have historically been employed in a variety of fields owing to the excellent mixing they provide, which can enhance chemical reaction rates and make the control of the reactor temperature easier than other technologies. Due to this wide application, heuristic knowledge of their functioning has been accumulating over the years. This knowledge, however, is not always backed by a deep understanding of the physical phenomena occurring in such systems. While this heuristic knowledge is sufficient to operate fluidized beds, operation optimization and scale-up are much harder to perform. A range of diagnostic techniques have been applied over the years to draw information about the inner workings of fluidized beds. Among these, x-ray imaging techniques, especially x-ray digital radiography and x-ray computed tomography, stand out for the kind and quality of information they can provide. Their high penetrating power enables visualization of phenomena taking place in the bulk of a fluidized bed, without disturbing the bed hydrodynamics. Furthermore, x rays are generated by a source that can be switched off, making them inherently safer than other imaging techniques relying on radioactive sources, such as γ-ray computed tomography. This work gives an overview of the techniques themselves, of the quantities they can measure, and of some modern applications of gas–solid fluidized beds they have been applied to, such as waste treatment and thermochemical conversion of biomass. Overall, x-ray digital radiography and x-ray computed tomography are better suited for process understanding than for process monitoring and are extremely useful in the study of voidage distribution and macro structures, such as bubbles and jets.

1. Introduction

Fluidized bed reactors play a key role in the chemical and process industries, especially for new applications in sustainable manufacturing and chemical recycling. Handling systems involving different classes of particles, gases and liquids are common in areas from the synthesis of fuels and chemicals to the treatment of wastes and specialty materials and carbon capture (Abanades et al., 2004; Iannello et al., 2020; Sebastiani et al., 2021; Yates & Lettieri, 2016).

Despite the wide usage of these multiphase systems, the methodology adopted for their design is still largely based on historical designs and rules of thumb rather than on first principles. The main reason for this is that the local flow structure is extremely complex and the link between the micro and macro-scale has not been established yet. Consequently, our understanding of the numerous hydrodynamic problems encountered with fluidized bed reactors remains incomplete. The lack of detailed structural and dynamic information, as well as the mathematical difficulties associated with the methods for handling the randomness of the particles, are the main reasons for the inability to treat these flows purely from a theoretical basis. The successful approach towards the understanding of such complex flows requires reliable data, which in turn depends on the implementation of sophisticated measuring techniques capable of non-invasive and non-intrusive investigation (Belchamber, 1995; Abdul Wahab et al., 2015). Among these techniques, x-rays represent one of the oldest, yet most promising ones (Chaouki et al., 1997; Grohse, 1955; Rowe et al., 1978).

X-rays are highly energetic electromagnetic radiation. Due to their high energy, they can penetrate objects and systems that are instead opaque to the visible light, enabling their study. They have been used for over 70 years in fluidization to distinguish between two distinct phases, where each phase has a significantly different x-ray attenuation coefficient. X-rays, although highly penetrating,

* Corresponding author.
E-mail address: massimiliano.materazzi.09@ucl.ac.uk (M. Materazzi).

https://doi.org/10.1016/j.partic.2023.11.013

undergo attenuation, which is a reduction in their intensity, due to the interaction phenomena of scattering, photoelectric absorption, and pair production with the medium they are traveling through. The level of attenuation can be linked back to properties of the imaged object, such as density and volume fractions of different phases (MacDonald, 2017). The first reported use of the technique was by Grohse in 1955 who measured the variation in density of a bed of silicon powder as a function of the fluidizing gas velocity (Grohse, 1955). In a three-phase system, multiple x-ray sources are typically operated at significantly different energy levels to differentiate each phase (Behling et al., 2006).

This article reviews the most recent use of x-ray visualization techniques to characterize multiphase flows in fluidized beds for new applications, especially those related to clean energy and sustainability. In particular, the emphasis is on two classes of x-ray imaging techniques: (a) x-ray digital radiography (XDR) and (b) x-ray computed tomography (XCT).

We begin by first discussing the basic principles of x-ray imaging in the two techniques. The different image processing techniques and hardware configurations are reviewed, as well as the methods for measuring the attenuation and the most important physical properties of the fluidized bed system (e.g., bed height, voidage, bubbles, etc.). For each technique, the experimental investigation of multiphase systems and fluidized beds is illustrated through a few examples, and some possible industrial and process applications are outlined. In presenting the above material we highlight our own personal experience in implementing x-ray imaging techniques for visualizing the phase distribution in fluidized-bed reactors of industrial interest.

2. X-ray digital radiography (XDR)

2.1. General overview

X-ray digital radiography (XDR) relies on x-rays being emitted from an x-ray source, traveling through the system under study, and being collected by an x-ray detector. As most x-ray detectors employed in XDR setups are 2D, the resulting image will be a 2D projection of a 3D object, where each pixel shows the cumulative attenuation over the corresponding x-ray path. Despite their high penetrating power, x-rays will face attenuation, especially when traveling through dense materials. This attenuation map can then be correlated to the phase distribution through which the beam corresponding to each pixel has travelled. This then allows hydrodynamic information to be determined (Lettieri & Yates, 2013; Yates et al., 2002). Fig. 1 shows a simplified schematic of an XDR setup for the observation of a gas-solid fluidized bed.

XDR has been widely employed to investigate fluidized-bed reactors. Grohse, Romero, and Rowe pioneered its use to study these systems in the 1950s–1960s (Grohse, 1955; Romero & Smith, 1965; Rowe & Partridge, 1965). These were also the first applications of non-invasive and non-intrusive diagnostic techniques to gas-solid fluidized-bed reactors. Technological progress enables constant improvement of spatial and temporal resolutions of x-ray imaging systems, reaching values as low as 400 nm and 40 ms when working with a reduced field of view (Jenneson & Gundogdu, 2006). It is worth mentioning that most setups employed nowadays for gas-solid fluidized beds rely on flash x-ray radiography (FXR). This consists in consecutive short but intense bursts of x-rays allowing capture of very fast events, such as the ones taking place in fluidized beds. Previously, x-rays were emitted continuously, allowing for smaller voltage requirements, but they were not capable of resolving most fluidization transients. The images are captured with digital detectors, which allow for

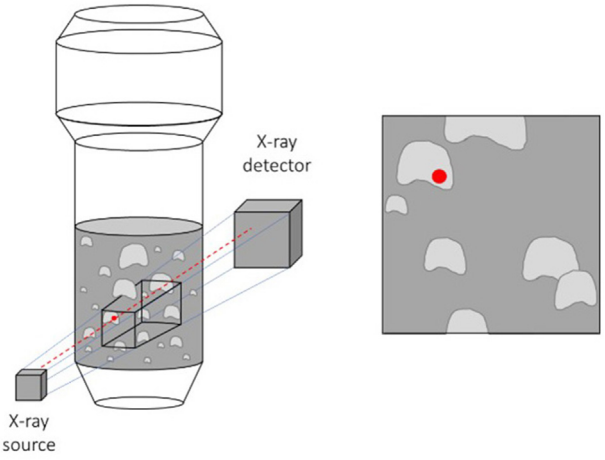

Fig. 1. Typical XDR setup for the observation of gas-solid fluidized beds. An x-ray source generates a beam of x rays that travels through the fluidized bed and is then collected by an x-ray detector (left). The resulting digitalized image is a 2D projection of the 3D fluidized bed, where each pixel on the detector gives information about the cumulative attenuation of the x-ray beam along the corresponding path (right).

larger acquisition speed and flexibility than the previous films. Some experimental setups were able to achieve frame rates as high as 1000 fps by coupling an x-ray system with a high-speed camera (Morgan et al., 2013). As the exposure time decreases, the brightness of the image also decreases, and this must be considered when designing the system. The x-ray source needs to provide sufficient energy for the images to be bright enough. Currently, most XDR systems operate with a spatial resolution in the 0.1–0.3 mm range and a temporal resolution between 0.05 ms and 3 ms, excluding the setup with a reduced field of view mentioned previously. Details of the equipment used by the researchers contributing the most to the knowledge of gas-solid fluidized beds using XDR in recent years are reported in Table 1. Nonetheless, a constantly improving observation of the phenomena taking place in fluidized-bed reactors is possible because of the high voltages and currents achieved in x-ray imaging systems, in the range of hundreds of kV and thousands of mA respectively (Ariyapadi et al., 2003), together with improvements in resolution. The voltage determines the energy of the x-rays and must be carefully adjusted to the application under study. If it is too low, most of the x-rays are attenuated, the images do not have enough contrast and the information that can be extracted is very limited. If the voltage is set to a too high value, on the other hand, some regions in the resulting images might be saturated and not provide quantitatively relevant data.

An important effect to consider is the beam hardening. The lower energy part of the x-ray spectrum is more easily attenuated, and this means that, as the x-ray beam travels through the fluidized bed, the x-ray energy spectrum is shifted towards larger energies, resulting in a decreased attenuation coefficient. If the x-ray beam is polychromatic, meaning that it contains a wide range of energies, then beam hardening corrections must be applied. These must all be applied while the images are being captured and consist in the employment of filters, an increase of the x-ray source voltage, or adopting a dual-energy approach (Hensler et al., 2016; Heindel, 2011).

It is worth noting that one of the contributions to x-ray attenuation is x-ray scattering, which not only reduces the intensity of the x-ray beam, but can also produce artifacts and noise in x-ray images. In most cases where x-rays are applied to gas-solid fluidized beds, however, their scattering can be safely ignored (Heindel, 2011).

Table 1
Most active researchers in the past 20 years using XDR on gas-solid fluidized-bed systems. Their equipment, fields of application and the quantities that they measured with XDR are briefly summarized.

Principal investigators	Institution	Equipment	Resolution	Applications	Quantities measured
Yates, Lettieri, Materazzi	University College London	• Cone-beam x-ray source: ◦ 150 kV max ◦ 450 mA max • 2D image-intensifier x-ray detector	• Spatial: ~0.2 mm • Temporal: 0.2 ms	• Effect of operating conditions on fluidization (Lettieri et al., 2001; Lettieri & Macrì, 2016; Macrì et al., 2019) • Fuel particle devolatilization and segregation in thermochemical conversion of waste and biomass feedstock (Iannello et al., 2023; Errigo et al., 2023; Iannello et al., 2022a, 2022b; Bruni et al., 2002) • Jets (Panariello et al., 2017; Panariello et al., 2022; Pore et al., 2015) • Nozzle design (Materazzi et al., 2017) • Probe intrusiveness (Tebianian et al., 2015) • Cross-validation of XDR (Pore et al., 2015)	• Bed height (Lettieri et al., 2001; Lettieri & Macrì, 2016; Macrì et al., 2019) • Minimum fluidization velocity (Lettieri & Macrì, 2016; Macrì et al., 2019) • Gas-solid distribution (Iannello et al., 2023; Tebianian et al., 2015; Materazzi et al., 2017; Iannello, Foscolo, & Materazzi, 2022) • Bubble properties (Iannello, Foscolo, & Materazzi, 2022) • Particle position (Errigo et al., 2023; Iannello, Bond, et al., 2022; Bruni et al., 2002) • Jet penetration length (Materazzi et al., 2017; Panariello et al., 2017; Panariello et al., 2022; Pore et al., 2015)
Kantzas	University of Calgary	• Cone-beam x-ray source: ◦ 120 kV max ◦ 1000 mA max • 2D image-intensifier x-ray detector	• Spatial: 0.1 mm • Temporal: not stated (30 frames/s)	• Bubble properties (Kantzas et al., 2001; Hulme & Kantzas, 2004) • Effect of pressure on bubbles (Orta et al., 2011) • Effect of the bed material on the fluidization (Wu, Kantzas, et al., 2007; He et al., 2007) • CFD validation (Hulme & Kantzas, 2005; He et al., 2007; Chandrasekaran et al., 2005)	• Bubble diameter, frequency and axial velocity (Kantzas et al., 2001; Orta et al., 2011; Wu, Kantzas, et al., 2007; He et al., 2007; Hulme & Kantzas, 2004)
Heindel	Iowa State University	• 2 x Cone-beam x-ray source: ◦ 200 kV max ◦ 10 mA max • 2 x 2D image-intensifier x-ray detector	• Spatial: ~0.2−0.3 mm • Temporal: 0.05 ms	• External object motion (Chen et al., 2019a; Drake, Tang, et al., 2009; Drake et al., 2008; Chen et al., 2019b) • CFD validation (Deza, Franka, et al., 2009)	• Tracer particle 3D position (Drake et al., 2009; Drake et al., 2008), distribution (Chen et al., 2019b) and orientation (Chen et al., 2019a) • Gas-solid distribution (Deza, Franka, et al., 2009)
Berruti, Briens	University of Western Ontario	• Cone-beam x-ray source: ◦ 125 kV max ◦ 1000 mA max • 2D image-intensifier x-ray detector	• Spatial: ~0.3 mm • Temporal: 3 ms	• Liquid injection (Ariyapadi et al., 2003; Ariyapadi et al., 2004) • Jets (Ariyapadi et al., 2003; Ariyapadi et al., 2004)	• Agglomerate tracking (Ariyapadi et al., 2003) • Jet penetration length and expansion angle (Ariyapadi et al., 2003; Ariyapadi et al., 2004)
Gundogdu, Jenneson	University of Surrey	• Cone-beam x-ray source: ◦ 60 kV max ◦ 0.1 mA max • 2D image-intensifier x-ray detector • Limited field of view (~24 mm × 32 mm)	• Spatial: 0.4 μm • Temporal: 40 ms	• Agglomeration of fluidized nano particles (Jenneson & Gundogdu, 2006; Gundogdu et al., 2007)	• Nanoparticle agglomerate size (Jenneson & Gundogdu, 2006; Gundogdu et al., 2007)

2.2. Image processing

Depending on the data the user is interested in, different image processing steps are required. However, the first ones, here referred to as pre-processing steps, are shared between all applications, whether the goal is to study bubbles and jets, track particles or calculate the voidage distribution in the fluidized bed. All the steps necessary for different x-ray image analyses are reported in Fig. 2 and explained in the following paragraphs.

2.2.1. Pre-processing

Most XDR setups rely on an image intensifier with a curved phosphor screen. This results in distorted images, and correction for pincushion distortion is necessary. This consists in applying a barrel distortion, the opposite of the pincushion distortion, to the raw x-ray frame in order to obtain an undistorted image. A grid with straight lines can be used to calibrate the barrel distortion parameters by varying these until the expected image of the grid is obtained. The pincushion distortion correction procedure is explained in detail in reference (Liu et al., 2009). Fig. 3(a) and (b) show, respectively, a raw x-ray image and an image corrected for pincushion distortion of a pseudo-2D fluidized bed. Although mostly used for research purposes rather than for industrial applications, this type of bed is excellent to visualize processing steps for x-ray images. However, the same procedures can be equally applied to 3D cylindrical fluidized beds as long as the x-ray images present a sufficient level of detail.

Once the image distortion has been corrected, the region of interest (ROI) is selected, and the x-ray images are cropped

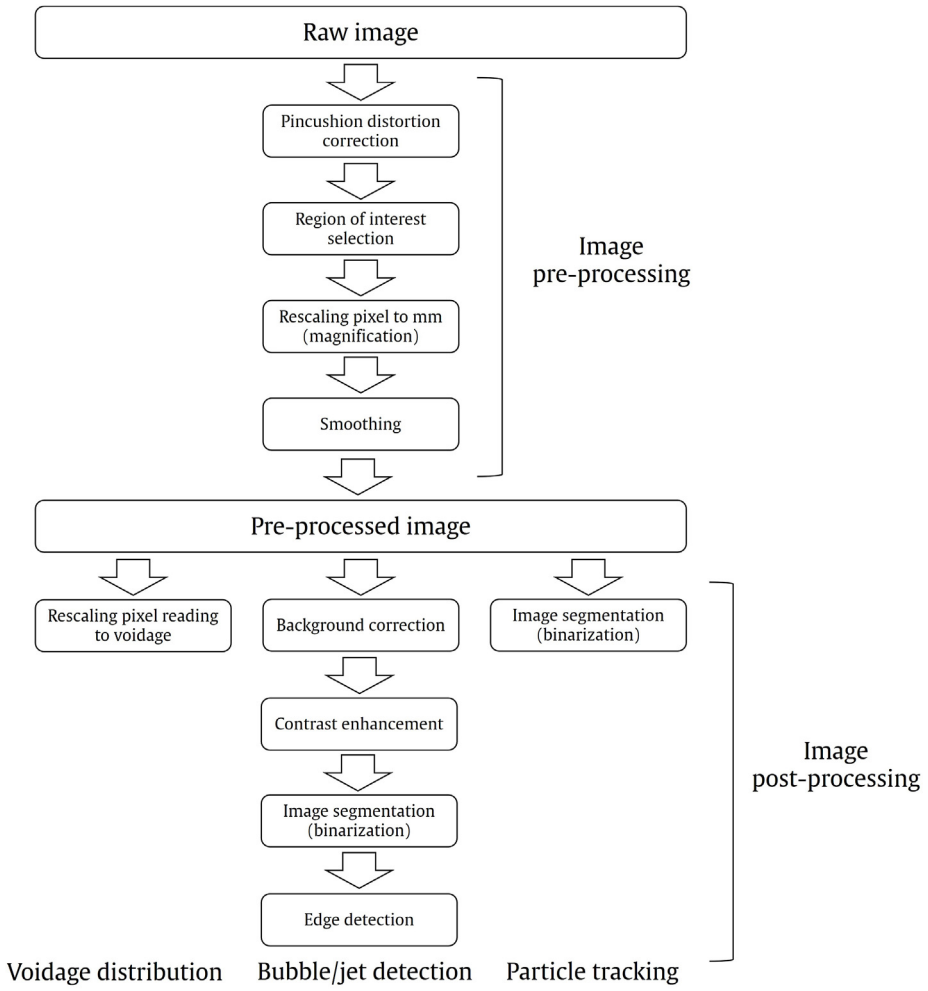

Fig. 2. Diagram showing the main processing steps, divided into pre-processing and post-processing, for XDR images. The first four steps are in common regardless of the application, but the last ones differ depending on whether the images are being used to detect bubbles and jets or to track particles, or if the goal of the study is to obtain a voidage distribution in the fluidized bed.

accordingly, as shown in Fig. 3(c). This reduces the amount of data to be processed, while preserving what can provide useful information.

The fact that x-rays diverge results in a magnification of the object studied on the x-ray detector. This magnification is more significant the closer the object is to the x-ray source. A simple

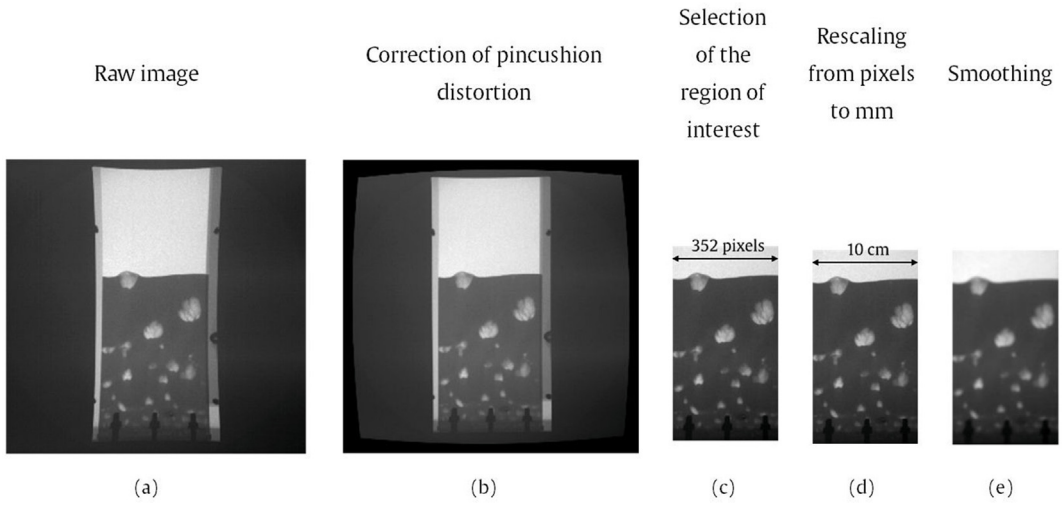

Fig. 3. Pre-processing steps for x-ray images of a pseudo-2D fluidized bed of rutile sand fluidized with air at $2U_{mf}$. These first steps are applied independently of the final goal of the analysis, whether the interest lies in obtaining a voidage distribution or in tracking bubbles, jets or particles. The darker regions at the bottom of the fluidized bed are bolts belonging to the fluidized bed vessel and are outside the bed itself.

geometric similarity can be used to obtain the actual object size, as showcased in Fig. 3(d), as long as either the source-to-object distance and the source-to-image distance, or the pixel-to-mm conversion factor are known. This latter can be obtained using a reference length, as done in reference (Iannello et al., 2023).

The last step shared among all applications of x-ray images is the smoothing of the images. Inevitably, the x-ray detector will pick some noise, which consists in casual variations in the pixel readings. In order to limit the effect of this phenomenon and reduce the noise-to-signal ratio, smoothing is performed. This consists in averaging the reading of multiple pixels, resulting in a more blurred image which, however, presents less noise artifacts. The effect of smoothing on the x-ray image can be observed by comparing Fig. 3(d) and (e), respectively before and after smoothing. This technique is also known as denoising or pixel binning. Although not strictly necessary for all applications, such as for x-ray particle tracking, it does improve the quality of the post-processed images in most cases.

Once this first set of steps has been performed, according to the goal of the analysis, different sets of post-processing techniques need to be applied to the x-ray images.

2.2.2. Post-processing for voidage distribution

If the aim is to obtain a voidage, or gas volume fraction, distribution, the attenuation map can be converted into it by applying the Beer-Lambert law:

$$I_i = I_0 e^{-\mu l_i} \tag{1}$$

where I_i is the attenuated intensity of the i-th x-ray path measured by the i-th pixel of the detector, I_0 is the x-ray intensity as the beam is emitted from the source, μ is the material attenuation coefficient and l_i is the length of material the x-rays have travelled through along the i-th path. Where x-rays cross different materials, the attenuation is cumulative and the exponential in Eq. (1) becomes a summation of the different lengths travelled by the beam in the different materials, each multiplied by the relative attenuation coefficients. For gas–solid mixtures, where the attenuation of x-rays in the gas can be neglected, this reduces to:

$$I_i = I_0 e^{-\mu_s l_i (1-\varepsilon)} \tag{2}$$

where μ_s is the attenuation coefficient of the bed material and ε is the average voidage along the i-th x-ray path. The volume fraction of the fluidized-bed phases in each pixel can then be calculated by using two reference x-ray images, one where the bed column is empty and one where the bed is packed. These two images, whose voidages are uniform and known, can be used to fit Eq. (2) and to obtain a value for μ_s, which then enables the calculation of the voidage distribution. This procedure applied to Fig. 3(e), and the resulting voidage distribution is reported in Fig. 4.

It is worth highlighting that, due to the nature of XDR, the obtained voidage is actually an average along a chord. However, if hydrodynamic structures (bubbles or jets) do not overlap in an XDR image and they are assumed to be axially symmetrical, which in many cases is an acceptable assumption, their voidage distribution can be obtained by adopting Abel's inversion method. This technique, based on the Tikhonov regularization, can be used to reconstruct the 3D density distribution of an axially symmetrical object starting from a 2D projection of the object itself. Since the densities of gas and bed material are significantly different, this density distribution can be converted into a voidage distribution. Abel's inversion method consists in dividing the field into annular elements of constant thickness and then solving for the voidage in each of these elements relying on the axial symmetry of the object

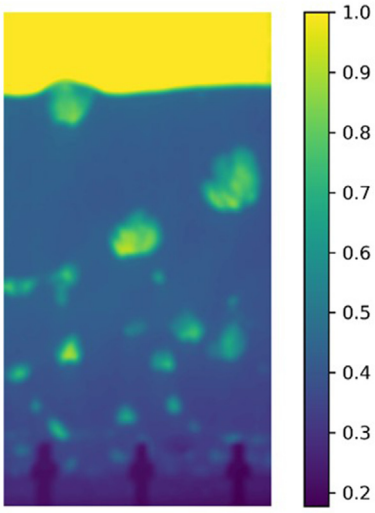

Fig. 4. Voidage distribution obtained from the x-ray image in Fig. 3 (pseudo-2D fluidized bed operated at $2U_{mf}$). The value of voidage in each point has been obtained by applying Eq. (2) to each pixel of Fig. 3(e) using the freeboard and the emulsion for normalization.

imaged. More details about the procedure are presented in reference (Wu et al., 2008). The great advantage of this technique is that it requires x-ray readings from one projection angle only to calculate a 3D voidage distribution.

If a cylindrical fluidized bed is under study and axial symmetry is assumed, Abel's inversion method can also be applied at a larger scale to obtain the whole bed voidage distribution. However, the assumption of axial symmetry for a cylindrical fluidized bed is only valid over large time scales and can therefore only be used for time-averaged measurements.

2.2.3. Post-processing for bubbles and jets

If the x-ray user is interested in following bubbles or jets in a fluidized bed, the post-processing steps are background correction, contrast enhancement, image segmentation and, finally, edge detection.

Since in most cases the geometry of fluidized beds is cylindrical, and the x-rays travel along paths with different lengths across the bed, x-ray images will present brighter and darker areas even when the bed is not fluidized. To correct for this, a fixed bed image can be used as a reference and subtracted from each frame in order to highlight only the differences from the packed state. If background correction is applied to Fig. 3(e), the image shown in Fig. 5(a) is obtained.

After this, the contrast in the image is enhanced to highlight differences between pixels and to make the image easier to process in the following steps. Although it cannot be easily seen, Fig. 5(b) shows the effect of contrast enhancement on Fig. 5(a).

Image segmentation aims to identify different regions within an image according to the characteristics of pixels. Most of the time this means binarizing the image by setting a threshold. This post-processing technique is also called binarization or thresholding. A value of thresholding, local or global, is selected, and the pixels are assigned a value of 0 or 1 depending on whether their value is larger or smaller than the selected threshold value. The resulting black-and-white image is shown in Fig. 5(c).

Finally, in order to characterize bubbles and jets, their edges are detected and their shape and size determined. This step is performed by implementing one of the multiple available edge-detection algorithms, such as the Sobel or the Canny edge-detection algorithms. Fig. 5(d) shows the result once this

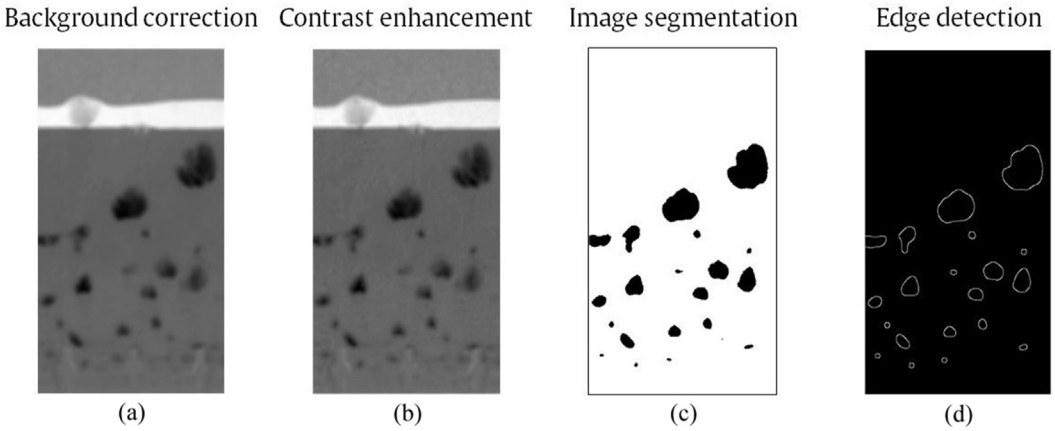

Fig. 5. Additional post-processing steps necessary to study bubbles and jets applied to Fig. 3(e) (pseudo-2D fluidized bed operated at $2U_{mf}$).

algorithm has been applied to the image resulting from image segmentation.

2.2.4. Post-processing for particle tracking

Finally, if the x-ray images are being used for x-ray particle tracking, not all of the last few steps are strictly necessary, and, most commonly, an image segmentation step, leading to a binarized image where the tracer particle is highlighted, is sufficient to identify the position of a tracer particle.

2.3. Fluidized beds characterization

2.3.1. Voidage distribution

Due to its operating principle, the most immediate variable of a fluidized-bed reactor that can be measured via XDR is the voidage distribution, where voidage means the gas volume fraction in a gas-solid fluidized bed. Due to the significant difference in density between gas and solid phases, the beam will undergo very different attenuation when passing through the different phases.

The voidage distribution and the fluidization quality depend strongly on some elements of the fluidized bed, such as the distributor plate used (Wormsbecker et al., 2009), internals, and the presence of intrusive probes (Tebianian et al., 2015). XDR proved to be a valuable tool in quantifying these effects. Fig. 6 shows the voidage distribution in a 3D fluidized bed, highlighting the impact on it of an intrusive optical probe. XDR has also been used for the characterization of voidage profiles in a downward-flowing fluidized bed (Cao & Weinstein, 2000).

2.3.2. Bed expansion

Whilst being a particularly important quantity in fluidized-bed reactors, the bed height during operation is not always simple to determine with sufficient accuracy. XDR can then be used to accurately evaluate the bed height and to study its evolution in time. Bed expansion (or collapse when reducing the gas flow rate) is critical to evaluate the behavior of different bed materials and their capacity to retain or permeate gas during operation. For example, the transient corresponding to a bed collapse test was used to investigate the effect of the temperature on the fluidization of group A particles using x-rays (Lettieri et al., 2001). The results of this work highlighted the difference in behavior between a bed material dominated by hydrodynamic forces and one dominated by interparticle forces. Furthermore, it was observed how high temperatures can cause a shift in the bed behavior from group A to group C, potentially leading to defluidization.

2.3.3. Bubble properties

A thorough understanding of bubble characteristics such as size, shape, and rise velocity is of fundamental importance in determining the behavior of a fluidized bed. XDR provides an

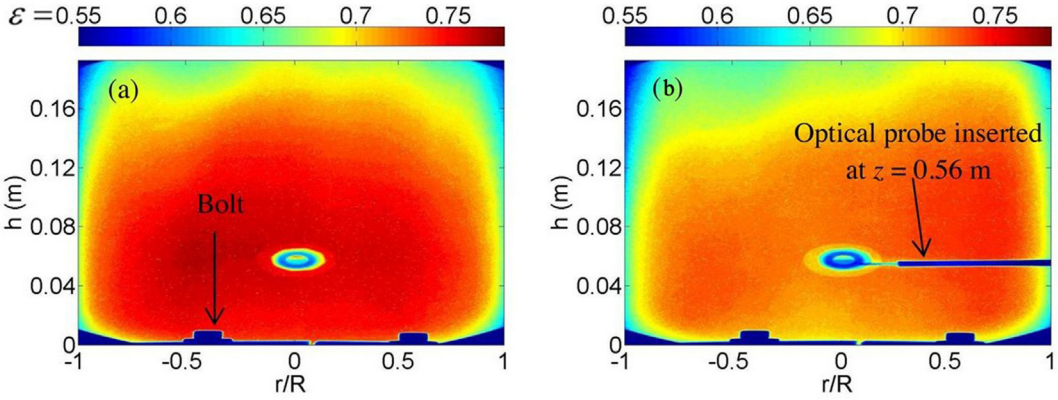

Fig. 6. Time-averaged voidage distribution in a vertical section of a cylindrical fluidized bed of silica sand fluidized with air at ~$6U_{mf}$ (a) without and (b) with an optical probe inserted. The effect of the intrusive probe on the voidage distribution is relatively limited, leading to a change in the average voidage over the region investigated <2%. The elliptical region in the center of both images does not belong to the probe but is another insertion port that has been closed off for this set of experiments. Image reproduced and adapted with permission from reference (Tebianian et al., 2015).

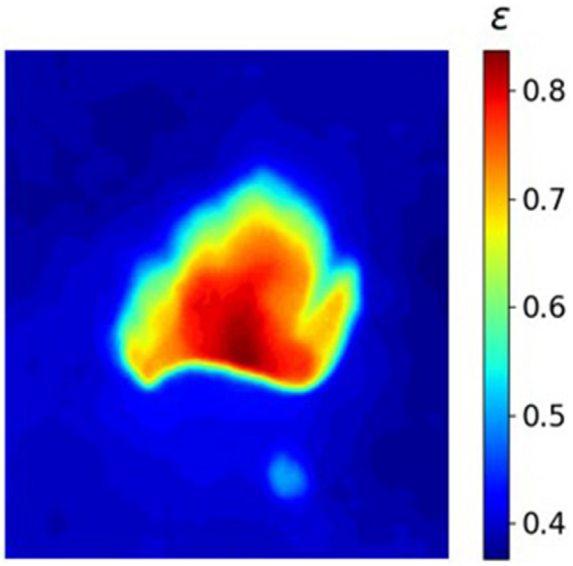

Fig. 7. Voidage distribution within and in the surroundings of a gas bubble in a pseudo-2D gas–solid fluidized bed obtained via XDR. The bed material is rutile with an average diameter of 215 μm, and it was fluidized with air at $2U_{mf}$. Some common features of gas bubbles in gas-solid fluidized beds can be observed, such as the bed material falling through the roof of the bubble, as well as the bubble wake, in the lower region of the bubble, dragging bed material upward together with the bubble itself.

excellent tool to do so, as shown in Fig. 7, as it allows direct observation of bubbles as they travel upwards in a fluidized bed. Nucleation, coalescence, and splitting of gas bubbles can then be studied experimentally. These cause significantly less attenuation than the emulsion phase and will result in the corresponding regions on the x-ray detector presenting larger x-ray readings. By using XDR, bubble size, frequency, and rise velocity were evaluated in different systems and under different operating conditions, such as temperature and pressure (Kantzas et al., 2001; Lettieri et al., 2001; Newton et al., 2001; Orta et al., 2011; Wu, Kantzas, et al., 2007). Furthermore, XDR allows observation of the voidage distribution within and in the surroundings of a bubble. This kind of information is extremely useful to characterize different regions of bubbles, such as the wake, the cloud and the bubble itself (Chaouki et al., 1997; Iannello et al., 2023). An accurate description of bubbles is fundamental for understanding their behavior and the effect of operating conditions on them, to model such behavior, and to validate computational fluid dynamics (CFD) modelling codes (Hulme & Kantzas, 2005; He et al., 2007; Chandrasekaran et al., 2005).

2.3.4. Jets

Many industrial applications of fluidized-bed reactors involve jets. These can be vertical or horizontal and can be used to inject the fluidizing gas from distributor nozzles, the liquid fuel stream, or both into a fluidized-bed reactor. These fluid-dynamic structures can significantly affect the fluidization quality of fluidized beds and their understanding must be well understood in order to guarantee optimal fluidization conditions. A study on horizontal jets proved that wall effects are the reason why the horizontal jet penetration length seems to be strongly related to the nozzle exit velocity (Newton et al., 2001). This implies that results on the jet penetration length obtained in a pseudo-2D fluidized bed cannot be directly assumed valid for 3D beds. As previously mentioned, some of these jets are used to inject liquid or a gas-liquid mixture into a fluidized-bed reactor such as in the case of fluidized catalytic cracking (FCC) reactors (Ariyapadi et al., 2003). In these cases, the risk for undesirable operational problems such as defluidization and channeling must be carefully considered. This injection may lead to the formation of liquid bridges between bed material particles, potentially leading to the formation of agglomerates. In the same study, (Newton et al., 2001), the authors also investigated the characteristics of the injection of liquid in fluidized beds, focusing on the dispersion of the spray and any differences between a spray in a fluidized bed and in open air. XDR allowed them to compare different nozzle designs and develop optimal ones. A further study (Ariyapadi et al., 2003) investigated the jet expansion angle and the penetration length, but, in this case, they compared gas-liquid and gas-only jets. Furthermore, through the use of radio-opaque tracers in the liquid feed, they investigated the formation and the behavior of agglomerates. However, relatively small quantities of tracer were used, and the raw images were not presented. It is then hard to appreciate how easily identifiable these tracers are. Nevertheless, the knowledge achieved, combined with theoretical modelling, allowed the same group to obtain a correlation for the penetration length of a gas-liquid horizontal jet (Ariyapadi et al., 2004). The same experimental setup was then used to validate the correlation. XDR has also been used to study how different novel nozzle designs can impact the properties of such jets and what configuration might be more beneficial for a specific application (Materazzi et al., 2017). Some of the resulting images are shown in Fig. 8. The same x-ray imaging system was then used to assess the effect of jet velocity, particle size, and particle density of a horizontal jet in a gas-solid fluidized, which was then condensed into a new non-dimensional correlation, and to validate a CFD model of a single horizontal jet (Panariello et al., 2017; Panariello et al., 2022).

2.3.5. Particle tracking

X-ray digital radiography has also been extensively used for the tracking of large particles in fluidized-bed systems (Chen et al., 2019a; Drake et al., 2008; Drake et al., 2009). This technique is better known as x-ray particle tracking velocimetry (XPTV). Once the x-ray images have been collected, an example is shown in Fig. 9, the processing is extremely similar to the one of particle tracking velocimetry (PTV). The main difference between XPTV and PTV, nevertheless, is the fact that the former allows particles to be tracked in the bulk of dense phases, such as the emulsion phase of a fluidized bed. PTV, on the other hand, is only suitable to track particles in dilute flows or in the periphery of a dense fluidized bed. XPTV, however, requires tracer particles which, to be identified, must differ in x-ray absorption properties from the bed material. This is usually achieved by doping them with a heavy material, such as lead or iron, as presented in reference (Drake et al., 2011). The resulting tracer particles are most of the time larger than the bed material particles and will therefore behave differently (Drake et al., 2008). Many fluidized-bed applications, however, deal with particles larger than the bed material particles, such as in the case of thermochemical conversion of biomass and plastic in fluidized-bed reactors. By means of techniques such as density matching, the location of a biomass particle can be followed in a fluidized-bed reactor operating at industrial process conditions (Errigo et al., 2023; Iannello, Foscolo, & Materazzi, 2022; Iannello, Bond, et al., 2022). When multiple source-detector pairs are available, stereoscopic XPTV can be performed, allowing observation of the orientation of non-spherical particles in fluidized beds (Chen et al., 2019a) and the granular temperature distribution in granular systems (Maranic et al., 2021).

2.4. Comparison with other techniques and models

Different diagnostic techniques can provide valuable details on fluidized bed dynamics and some of them have been used together

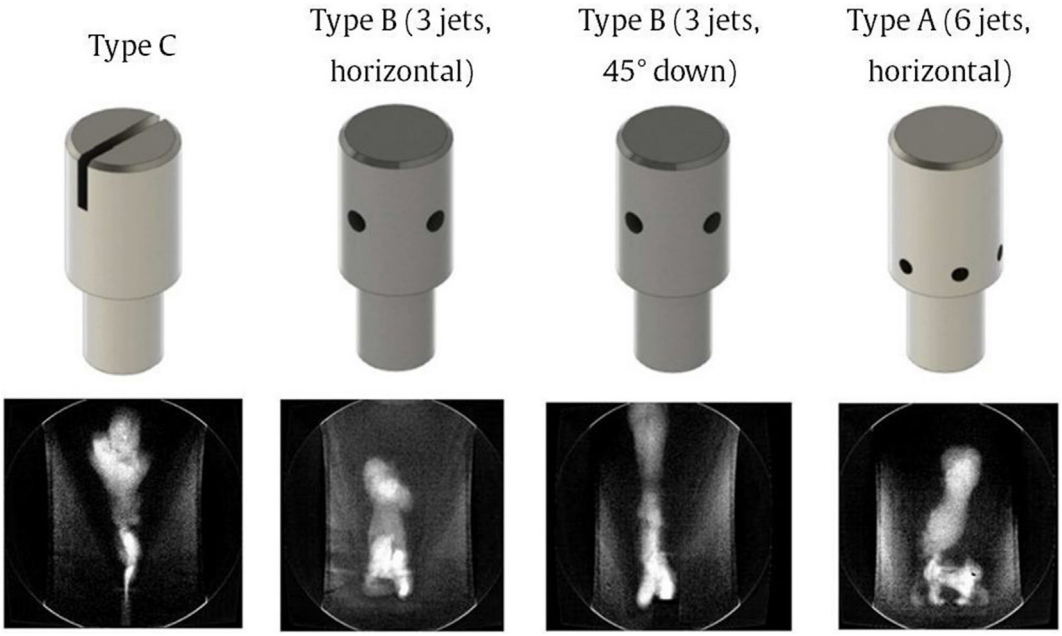

Fig. 8. Different nozzle designs and corresponding x-ray images of the jets generated by them in a cylindrical fluidized bed with a diameter of 150 mm, fluidizing silica sand with air at 90 l/min. The x-ray images allowed the authors of reference (Materazzi et al., 2017) to determine what nozzle design would perform better in terms of plume stability, lateral penetration and gas distribution in thermal de-nitration fluidized-bed reactors. Image reproduced and adapted with permission from reference (Materazzi et al., 2017).

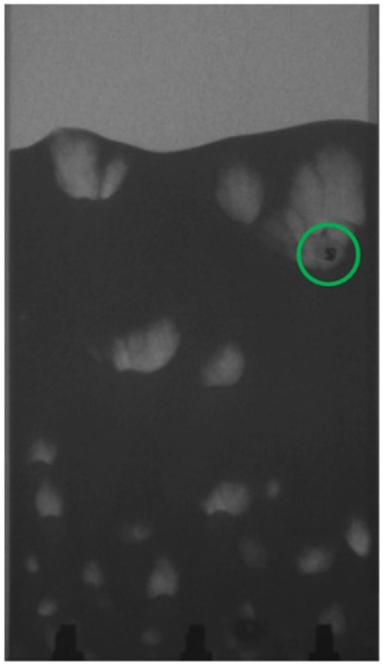

Fig. 9. X-ray image of a pseudo-2D fluidized bed of rutile sand fluidized with air at $2U_{mf}$ for XPTV. The tracer particle has been highlighted with a green circle and it is made up of an iron core and a polypropylene shell. Attenuation of x-rays through iron is sufficiently larger than in the emulsion phase for it to be identified in each frame and tracked. This is the principle behind XPTV.

with XDR to characterize some specific properties and validate theoretical models. This allowed cross-validation of XDR with these other techniques. XDR was used to observe vertical jets in a packed bed and to cross-validate the technique with MRI and PEPT (Pore et al., 2015). The three techniques were found to be in very good agreement, with minor discrepancies for the x-ray measurements at low flow rates, probably due to limitations in the minimum detectable void. Further validation of XDR was carried out against a range of techniques including electrical capacitance tomography and radioactive particle tracking (Tebianian et al., 2015), that had been previously applied to the same experimental setup by other researchers (Dubrawski et al., 2013). Once again, the results obtained satisfactorily matched the ones in the literature.

As previously mentioned, XDR can be a useful tool for the validation of CFD codes. A two-phase model, for example, was used to study the bubble behavior and interaction in a 3D cylindrical fluidized bed and in a pseudo-2D one respectively (Hulme & Kantzas, 2005; He et al., 2007). The results were then validated against XDR measurements in terms of average bubble diameter, rise velocity, and bubble size distribution. Notable differences were observed in both cases, highlighting the need to refine the capabilities of Eulerian-Eulerian simulations of fluidized beds. XDR can also be used in combination with other diagnostic techniques (Chandrasekaran et al., 2005). In this study, the technique was combined with pressure fluctuation analysis to validate the CFD model of a fluidized bed of non-ideal polyethylene particles. A significant difference from previous work is that the authors used time-resolved information on bubbles for the validation. The results stressed the need for a better characterization of the simulation solids properties for polyethylene. Because of the Eulerian nature of the data obtained through XDR, this technique is more suitable to validate Eulerian CFD models. Simulations relying on the discrete element method (DEM) might be better validated by Lagrangian techniques such as positron emission particle tracking (PEPT) or magnetic particle tracking (MPT). As the computational power of computers increases exponentially, it seems that CFD-DEM models will be the way forward, and, in this, XDR can still play a role in terms of validation, but mostly for Eulerian quantities.

2.5. Applications

The capability of XDR to observe the voidage distribution, the bed height, as well as bubble and jet properties, through

stainless steel walls has enabled researchers to investigate phenomena occurring at industrial operating conditions. This is extremely important, as, although scaling rules exist (Glicksman et al., 1994), the reliability of these is still very much under debate (Knowlton, 2013), and not always are the lab-scale experimental results directly translatable to larger scales. Furthermore, the simultaneous scaling of different physical aspects involved in fluidized beds is impossible to achieve in practice (Leckner et al., 2011). For this reason, experiments run at industrial operating conditions are extremely valuable in predicting the behavior of industrial fluidized-bed reactors as well as in validating the scaling rules. The group at University College London (UCL) led by Lettieri and Materazzi has been focusing on assessing the impact of operating conditions on fluidized-bed reactor operation. XDR has been used to follow the bed height evolution in bed collapse tests and to determine minimum fluidization velocities. This information enabled the investigation of the impact of process conditions on the behavior of fluidized-bed reactors (Yates & Lettieri, 2016; Lettieri et al., 2001; Lettieri & Macrì, 2016; Macrì et al., 2019). While these works mostly analyzed the effect of temperature and of the presence of fines, some complementary studies (Orta et al., 2011) aimed to quantify the effect of pressure on the fluidization quality. The research group at UCL also intensively studied the thermochemical conversion of waste and biomass feedstock investigating both exogenous and endogenous bubbles. While the first ones are formed by the fluidizing gas, and are an intrinsic feature of bubbling fluidized beds, the latter ones are generated from the volatile matter in the feedstock during thermally induced devolatilization. Accounting for endogenous bubbles is extremely important for highly volatile feedstock, as these bubbles apply an additional lift force on the feedstock particles, affecting their segregation behavior and, therefore, their interaction with the fluidized bed. XDR proved to be an excellent tool to characterize both types, the interaction between them, and to track fuel particles (Iannello et al., 2023; Iannello, Foscolo, & Materazzi, 2022; Iannello, Bond, et al., 2022; Bruni et al., 2002). Both the endogenous bubble and the tracer fuel particle can be seen in Fig. 10. In one of these studies (Bruni et al., 2002), the authors run the reactor at incipient fluidization conditions, that is without formation of exogenous bubbles, in order to observe endogenous ones only and their effect on the trajectory of fuel particles. Some of the results showed fast segregation of feedstock particles towards the top region of the bed, which must be avoided in order to prevent the volatiles from bypassing the bed. The other studies, (Iannello et al., 2023; Iannello, Foscolo, & Materazzi, 2022; Iannello, Bond, et al., 2022), on the other hand, characterized the structure of endogenous bubbles generated by fuel particle devolatilization during initial pyrolysis and proposed a model for the lift force caused by them and acting on the fuel particle. This information is key to designing adequate feeding systems and reactor configurations for the newest application of fluidized beds in chemical recycling and waste management.

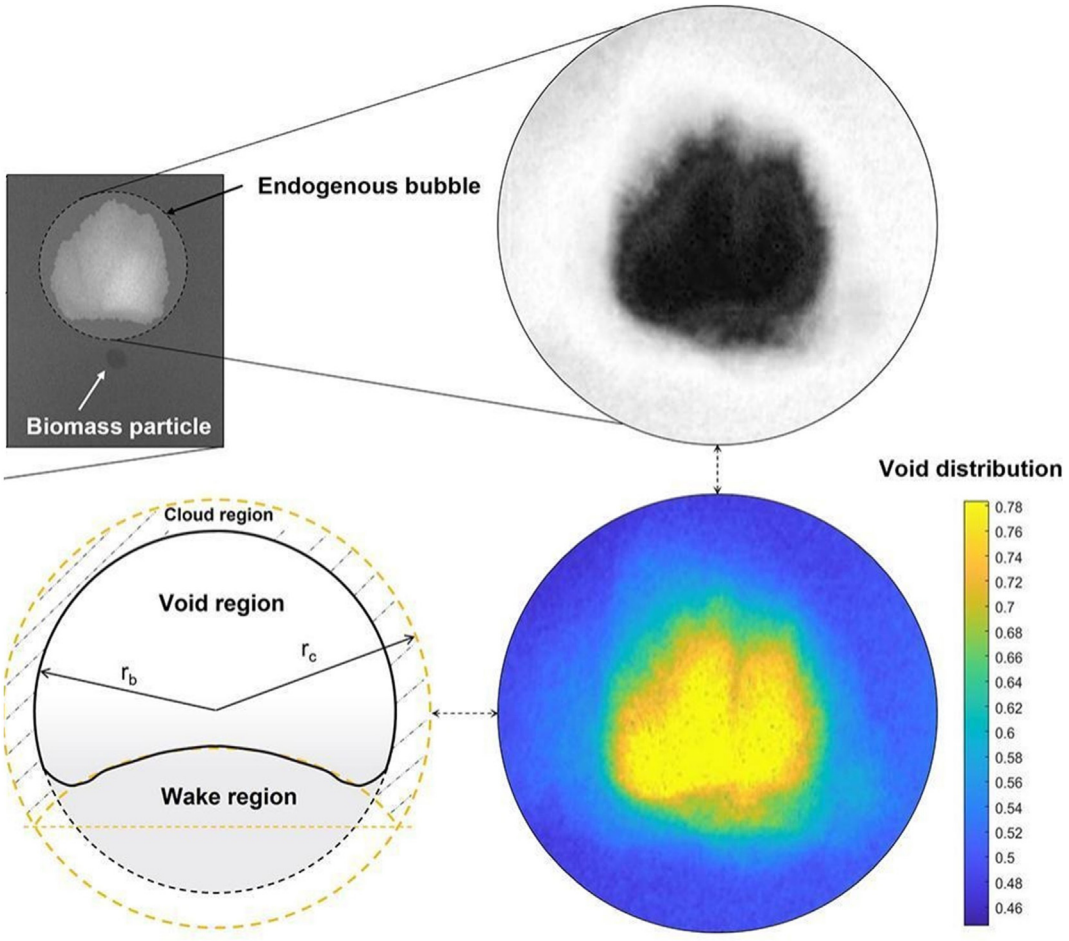

Fig. 10. Raw x-ray image and post-processed versions of an endogenous bubble produced by devolatilization of a biomass particle in a fluidized bed of quartz sand fluidized with nitrogen at U_{mf}. The image is captured, post-processed, and converted into a voidage distribution map. The different areas, wake, void and cloud regions can then be identified. Image reproduced with permission from reference (Iannello et al., 2023).

Table 1 reports the principal investigators that have most contributed in recent years to the current understanding of gas–solid fluidized-bed systems using XDR. Also some characteristics of the equipment they have available and the applications they focused on are presented.

3. X-ray computed tomography

3.1. General overview

X-ray computed tomography (XCT) also relies on the attenuation of x-rays through an object or a system to obtain information about the object, or system, composition. In the case of fluidized beds, the composition can be directly linked to the voidage distribution. Differently from XDR, however, XCT combines several x-ray projections together in order to reconstruct the density distribution in the bed cross sections, while XDR relies on a single projection only and does not directly provide a distribution. By overlapping the information collected from different directions, XCT allows for the detection of details that would otherwise be flattened onto the single projection if using x-ray absorption. Since cylindrical geometry is the most common in industrial fluidized beds and lends itself very well to the application of XCT, most studies employ XCT on cylindrical fluidized beds. Depending on the type of x-ray source and detector, XCT can be fan-beam 2D time-resolved XCT or cone-beam 3D time-averaged XCT (Heindel, 2011). The first one relies on fan beams and 1D detector arrays to return time-resolved horizontal slices of an object (Fig. 11). The most common configurations for this application are XCT systems with multiple source-detector pairs (Mudde, 2010a) and XCT systems relying on the electronic deflection of an electron beam (Fischer et al., 2008). On the other hand, cone-beam 3D time-averaged XCT uses cone beam x-ray sources and 2D x-ray detectors to capture the different time-averaged projections which are then combined together. This latter configuration has been used less often due to its inability to resolve transients. Most systems applying this technique rely on rotating XCT systems (Heindel et al., 2008). These main XCT setups are shown in Fig. 12. By increasing the number of x-ray sources, more accurate XCT images can be obtained (van Ommen & Mudde, 2008). However, this comes at the price of an increasing cost of the setup, as well as of a computationally heavier image processing.

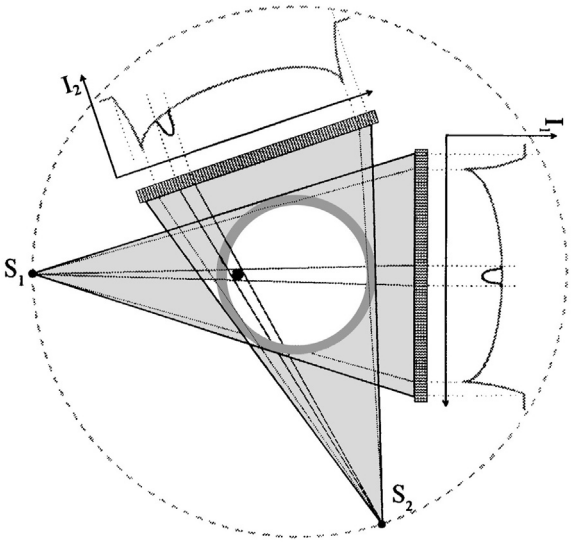

Fig. 11. Operating principle of x-ray computed tomography applied to a gas-solid fluidized bed. Different x-ray projections of an object are captured at different angles. Image reconstruction algorithms are then employed to calculate an attenuation map of the object. This attenuation map can be directly linked to the phase distribution in the investigated domain as emulsion and bubbles produce very different x-ray attenuation. Image reproduced with permission from reference (Grassler & Wirth, 2000).

Current XCT setups can reach spatial resolutions below the millimeter, with some time-averaged systems going as low as 80 μm. The temporal resolution strongly depends on the design. Rotating source-detector systems require a time in the order of seconds to perform a scan, which is then time-averaged. Multi-source setups, on the other hand, can go as low as a few milliseconds. And, finally, the ultrafast XCT setup developed at the Helmholtz-Zentrum Dresden-Rossendorf can reach a temporal resolution of 0.125 ms. Table 2 outlines research groups using XCT who mostly contributed to studying gas-solid fluidized beds and the characteristics of their setups.

Since its introduction, XCT has been applied to a wide variety of fluidized systems, including, but not limited to, bubbling (Ma et al., 2019), circulating (Hensler et al., 2016), and gas-liquid-solid fluidized beds (Gehrke & Wirth, 2005). Even though the application of XCT to the medical field began several decades ago, the technique was only applied to fluidized beds in the 1990s (Kantzas, 1994). While the spatial resolution has not been a limiting factor from the very beginning, the capabilities of XCT in terms of temporal resolution significantly improved in the last three decades. The first system used to study fluidized beds could not go below 3 s (Kantzas, 1994), and therefore could not capture time-resolved images, while more recent systems reached temporal resolutions as low as 0.125 ms (Bieberle & Barthel, 2016). The introduction of XCT systems without moving parts, such as the one described in reference (Bieberle, Fischer, et al., 2010), made this sharp increase in temporal resolution possible and enabled researchers to use them for the investigation of multiphase flows (Fischer et al., 2008; Mudde et al., 2008; Bieberle et al., 2007). The main limiting factor for the temporal resolution of XCT at the moment is the image reconstruction, especially for on-line use. The current technology allows 2D time-resolved or 3D time-averaged XCT measurements. However, the recent significant progress in computing power, and the appearance of graphic processing units (GPUs), are promising for real-time XCT applications (Bieberle et al., 2017) and for 3D time-resolved XCT, such as the one proposed in reference (Stürzel et al., 2011).

As XCT relies on multiple XDR projections, it is equally affected by x-ray scattering and beam hardening. Similar to as for XDR, most commonly the effect of x-ray scattering can be neglected (Heindel, 2011).On the other hand, beam hardening must be accounted for, and, to do so, calibration methods, such as the one presented in reference (Hensler et al., 2016) based on pre-filtration of the x-ray beam, can be employed.

3.2. Image processing

Similar to as for XDR, depending on the type of application, different post-processing techniques will be required. These are outlined in Fig. 13 and explained in the following paragraphs.

3.2.1. Domain breakdown

The first step in the reconstruction of the object image consists in breaking down the domain, a volume in the case of cone-beam 3D time-averaged XCT and a plane in the case of fan-beam 2D time-resolved XCT, into smaller elements, voxels and pixels respectively. An image reconstruction algorithm is then used to calculate a value of attenuation coefficient for each element, and, since this is directly linked with the element density, a density distribution, and therefore a phase distribution, can be obtained (Heindel, 2011).

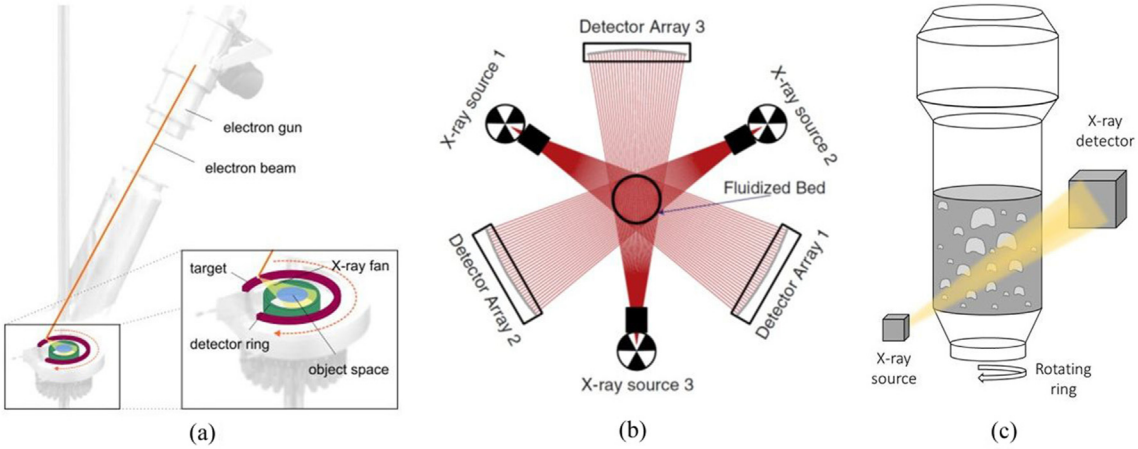

Fig. 12. Different configurations of XCT setups: (a) fan beam and 1D detector ring with electronic deflection of the electron beam, (b) fan beam and 1D detector arrays with multiple source-detector pairs, (c) cone beam and 2D detectors with the fluidized bed mounted on a rotating platform. Images reproduced and adapted with permission from references (Bieberle et al., 2012; Yang et al., 2014a).

Table 2
Most active researchers in the past 20 years using XCT on gas–solid fluidized-bed systems. Their equipment, fields of application and the quantities that they measured with XCT are briefly summarized.

Principal investigators	Institution	Equipment	Resolution	Applications	Quantities measured
Heindel	Iowa State University	2 rotating source-detector pairs (360 projection angles): • Cone-beam sources: ◦ 200 kV max ◦ 10 mA max • Detectors available: ◦ Image intensifier + CCD camera Phosphor screen + cooled CCD camera	• Spatial: 0.5 mm • Temporal: 45 min (time-averaged)	• Validation of CFD codes (Deza, Franka, et al., 2009; Min et al., 2008; Bai et al., 2013; Deza & Battaglia, 2015; Deza et al., 2011; Min et al., 2010) • Effect of bed material and bed height on the bed hydrodynamics (Escudero & Heindel, 2011; Drake & Heindel, 2012; Franka et al., 2007) • Observation of hydrodynamic regions (Drake & Heindel) • Effect of acoustic intervention on bed hydrodynamics (Escudero & Heindel, 2014a; Escudero & Heindel, 2014b) • Effect of probes on fluidization (Whitemarsh et al., 2016) • Devolatilization of biomass (Franka & Heindel, 2009; Drake & Heindel, 2012; Deza, Battaglia, & Heindel, 2009) • Jetting (Franka & Heindel, 2009; Escudero & Heindel, 2016) • Effect of side-port injection on fluidization quality (Deza et al., 2011; Deza & Battaglia, 2015)	• Time-averaged 2D voidage distribution on horizontal and vertical planes: local (Escudero & Heindel, 2011; Escudero & Heindel, 2014a; Whitemarsh et al., 2016; Franka & Heindel, 2009; Drake & Heindel, 2012; Deza, Battaglia, & Heindel, 2009; Deza et al., 2011; Franka et al., 2007) and averaged over annuli (Drake & Heindel) • Time-averaged 1D voidage profiles along radius and height: within slices (Deza, Franka, et al., 2009; Escudero & Heindel, 2014a; Whitemarsh et al., 2016; Drake & Heindel, 2012; Deza et al., 2009b, 2011; Min et al., 2010) and averaged over slices (Deza, Franka, et al., 2009; Escudero & Heindel, 2011; Escudero & Heindel, 2014a; Deza, Battaglia, & Heindel, 2009; Min et al., 2010; Deza et al., 2011) • Jet penetration length and expansion angle (Escudero & Heindel, 2016)
Mudde, van Ommen	Delft University of Technology	3 static source-detector pairs (3 projection angles): • Fan-beam sources: ◦ 150 kV max ◦ 12 mA max • Detector arrays: ◦ 2 rows (4 cm apart)	• Spatial: 3.5 mm • Temporal: 4 ms	• Effect of inter-particle forces on bubbles and slugs (Ma et al., 2019; Ma et al., 2021) • Effect of internals on bubble properties (Maurer et al., 2015a; Schillinger et al., 2017; Maurer, Wagner, et al., 2015)	• Number, frequency, size and velocity of bubbles and slugs (Mudde, 2010a; Ma et al., 2019; Mudde, 2010b; Ma et al., 2021; Brouwer et al., 2012; Maurer, Wagner, et al., 2015; Maurer et al., 2016)

(*continued on next page*)

Table 2 (*continued*)

Principal investigators	Institution	Equipment	Resolution	Applications	Quantities measured
		◦ 32 scintillation detectors per row		• Effect of operating conditions on fluidization (Brouwer et al., 2012) • Correlations for bubble size and bubble rise velocity (Maurer et al., 2016) • Validation of diagnostic techniques (Schillinger et al., 2018) • Effect of bed material shape on fluidization (Mema et al., 2020) • Jet regions (Yang et al., 2014a)	• Voidage distribution in a horizontal plane (Yang et al., 2014a)
Kantzas	University of Calgary	Rotating source and stationary detector system (number of projection angles not stated): • Fan-beam source: ◦ 140 kV max ◦ Up to at least 100 mA (max not stated) • Detector array: ◦ 900 detectors arranged in a circle	• Spatial: 0.5 mm • Temporal: 2 s (time-averaged)	• Effect of intrusive probes on voidage distribution (Dubrawski et al., 2013) • Effect of scaling and of the operating conditions on the bed hydrodynamics (Kantzas et al., 2001; Wu, Yu, et al., 2007) • Determination of the fluidization regime (Wright et al., 2001) • Validation of other diagnostic techniques (Chaplin et al., 2005)	• Voidage distribution in a horizontal plane (Kantzas et al., 2001; Dubrawski et al., 2013; Wu, Yu, et al., 2007; Wright et al., 2001; Chaplin et al., 2005) • Bubble size, velocity, number and frequency (Wu, Yu, et al., 2007; Wright et al., 2001)
Barthel, Hampel	Helmholtz-Zentrum Dresden-Rossendorf	Electronically deflected electron beam system: • Circular tungsten target producing x-rays: ◦ 150 kV max ◦ 65 mA max • 2 parallel circular x-ray detectors: ◦ 432 elements	• Spatial: 1 mm • Temporal: 0.125 ms	• Concentration and motion of particles in a spout fluidized bed (Bieberle & Barthel, 2016) • Effect of bed material, fluidization velocity and bed height on bubble properties (Verma et al., 2014)	• Voidage distribution in a horizontal plane (Bieberle, Fischer, et al., 2010) and in 2 parallel horizontal planes (Bieberle & Barthel, 2016) • Local particle velocities (Bieberle & Barthel, 2016) • Bubble size and velocity (Verma et al., 2014)
Wirth, Arlt	Friedrich-Alexander-Universität Erlangen-Nürnberg	Rotating source-detector system (1000 projection angles): • Fan-beam source: ◦ 140 kV max ◦ Up to at least 2.8 mA (max not stated) • Detector array: ◦ 5566 scintillation detectors arranged in a line	• Spatial: 80 μm • Temporal: 1 s (time-averaged)	• Effect of jet velocity, fluidization velocity and particle size on voidage distribution in a jet (Koeninger et al., 2018) • Entrainment of bed material in a jet (Koeninger et al., 2017)	• Voidage distribution in a horizontal plane (Koeninger et al., 2017; Koeninger et al., 2018)

3.2.2. Image reconstruction algorithms

The pre-processing of XCT data is not as straightforward as for XDR and, importantly, there are multiple reconstruction algorithms. The most commonly used one is the filtered back-projection (FBP) algorithm. This consists in taking the equation that describes the intensity of the projection as a function of the distance from the origin of the reference system and of the angle with respect to it, and reversing it (Eq. (3)). In the reversal process, a filter kernel is added to limit the blurring of the reconstructed image, where different filters are used for different applications.

$$\mu(x,y) = \int_0^{\pi} \int_{-t_{min}}^{t_{max}} p(\theta,a)\, h(x\cos\theta + y\sin\theta - a)\, da\, d\theta \tag{3}$$

where μ is the x-ray attenuation coefficient in position (x,y), θ and a are the x-ray orientation angle and the distance from the origin of the reference frame respectively, and h is the filter kernel (Lau et al., 2018). The FBP algorithm is particularly sensitive to the ill-posed nature of XCT. The pixels, or voxels, forming the attenuation map are significantly more than the number of data collected at each instant (Kantzas, 2022).

One other common reconstruction algorithm is the simultaneous algebraic reconstruction technique (SART), which starts from an initial guess and iteratively corrects it until a satisfying level of accuracy is reached (Lau et al., 2018; Yang et al., 2014b). The algorithm can be written as:

$$\alpha_j^{k+1} = \alpha_j^k + \frac{1}{\sum_{i=1}^{N} A_{ij}} \sum_{i=1}^{N} \left(\frac{b_i - \tilde{b_i}}{\sum_{j=1}^{M} A_{ij}} A_{ij} \right) \tag{4}$$

where α is the solid volume fraction, k is the iteration index, j is the pixel index, i is the beam index, A_{ij} is the weighing of the i-th x-ray path in the j-th pixel, b_i is the fraction of the path travelled by the i-th x-ray that is occupied by solids, and $\tilde{b_i}$ is defined as:

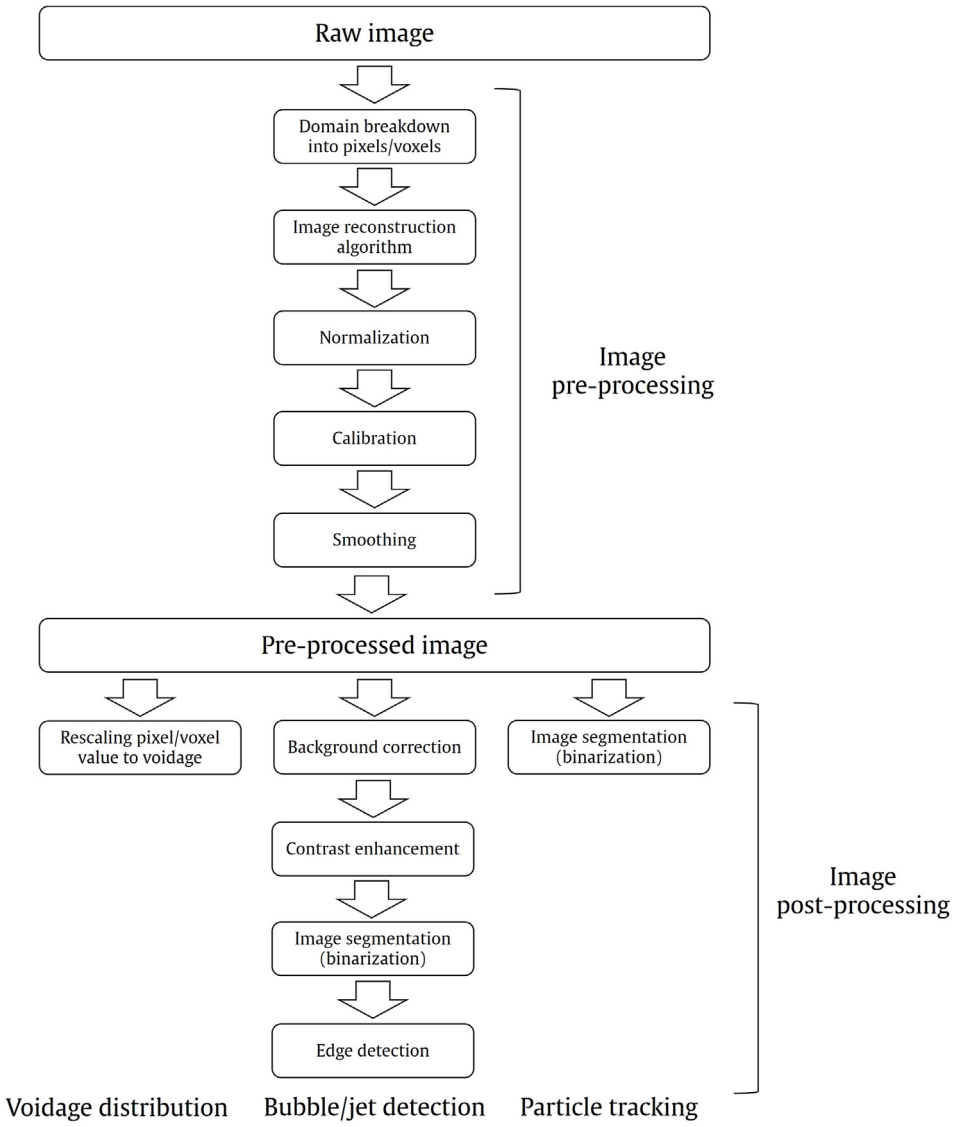

Fig. 13. Diagram showing the main processing steps, divided into pre-processing and post-processing, for XCT images. The first five steps are in common regardless of the application, but the last ones differ depending on whether the images are being used to detect bubbles and jets or to track particles, or if the goal of the study is to obtain a voidage distribution in the fluidized bed.

$$\tilde{b_i} = \sum_{j=1}^{N} A_{ij}\alpha_j \tag{5}$$

The SART algorithm is an improved version of the Algebraic Reconstruction Technique (ART) in that it corrects each pixel with the information drawn from all rays simultaneously (Yang et al., 2014b). Validation of these image reconstruction algorithms is typically done by using them to image a known configuration, usually involving a phantom, which is a test object whose size and density are known (Heindel, 2011; Lau et al., 2018).

When XCT relies on a fan x-ray beam, all projections taken from different angles can be combined into a sinogram, which consists in the layering of these consecutive projections next to each other. Fig. 14 shows an example of what a sinogram looks like for two phantoms in a cylindrical fluidized bed.

More recently, genetic algorithms have been used to reconstruct the object image with promising results. This algorithm generates a group of random solutions as initial guesses and then ranks them according to a fitness value. The ones deemed to be more fit will be more likely selected to be carried forward onto the next generation. The selected solutions are then mixed and some parts of them are randomly changed (cross-over and mutation steps respectively). This procedure is then repeated until a satisfyingly accurate solution is found (Yang et al., 2014b). The performances of the FBP algorithm and of the AGA algorithm, a modified genetic algorithm, were compared in reference (Wu, Cheng, et al., 2007), proving the suitability of the latter to image bubbles in a gas-solid fluidized bed and its increased performance with respect to the FBP in terms of robustness to noise and to bubble shapes. A comparison between the performances of the two techniques can be observed in Fig. 15. Both the genetic algorithm and SART are classified as optimization problems. The performances of the AGA were also compared to the SART algorithm (Yang et al., 2014b), and it was found that the first one performed better in terms of structural similarity index measure (SSIM) for coarser grids, while similar performances were achieved as the grid was refined beyond 30x30. This trend can be observed in Fig. 16. However, the AGA algorithm was also found to

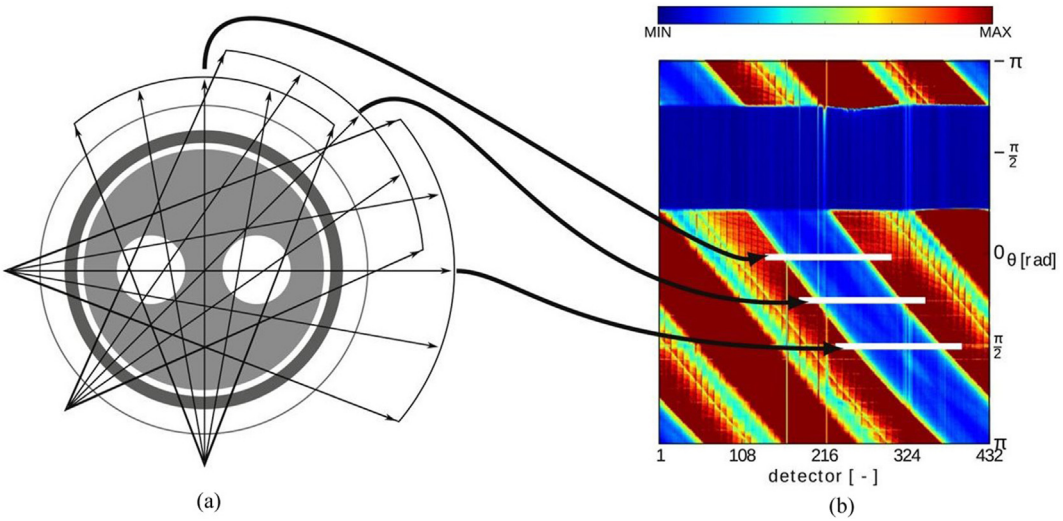

Fig. 14. (a) XCT projections and (b) sinogram of a horizontal slice of a cylindrical fluidized bed with two phantoms. A sinogram consists in placing the 1D x-ray projections captured to perform XCT next to each other and is post-processed into an attenuation map of the horizontal slice via image reconstruction algorithms. The data was captured with an ultra-fast fan-beam XCT setup characterized by electronic deflection of an electron beam (Fig. 12(a)). Image reproduced with permission from reference (Lau et al., 2018).

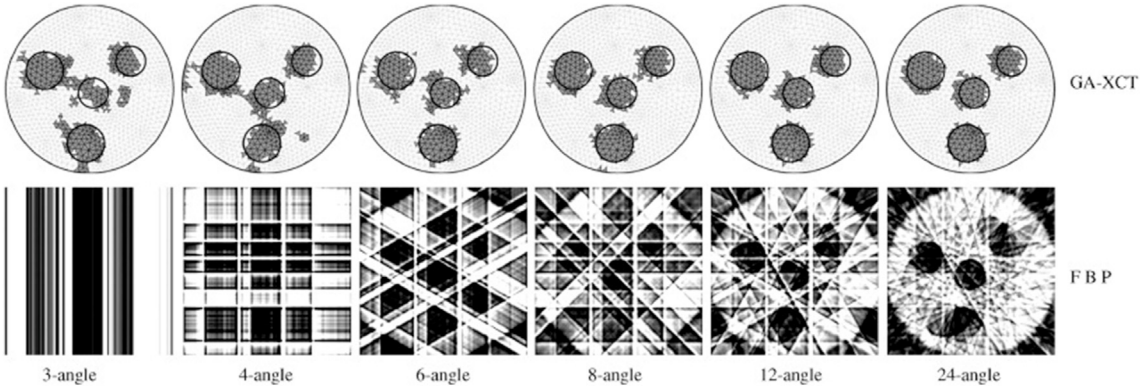

Fig. 15. Reconstructed images of a 90 mm polymethyl methacrylate (PMMA) vessel with four test-tubes, or phantoms, reproducing bubbles in a gas-solid fluidized bed and water acting as the emulsion phase. The first row of images shows the results obtained with the GA-XCT image reconstruction algorithm presented in (Wu, Cheng, et al., 2007), while the images in the second row were obtained following the more classical FBP algorithm. Each column shows the results corresponding to a different number of projection angles. The data was obtained from simulated experiments adopting an XCT system relying on multiple 1D source-detector pairs, such as the one in Fig. 12(b), with a varying number of pairs. Image reproduced with permission from reference (Wu, Cheng, et al., 2007).

be significantly more computationally expensive, even though there is some room for optimization. Furthermore, it was found to be not very consistent between different runs on the same experimental data.

To the authors' best knowledge, an extensive and systematic review comparing the performances, both in terms of accuracy and in terms of computational cost, of different image reconstruction algorithms for XCT has not been performed yet. This study, however, could be extremely beneficial to researchers employing XCT to investigate gas-solid fluidized beds.

A new model called mean intensity ratio reconstruction (MIRR) has recently been proposed (Gómez-Hernández et al., 2016). Even though it is not as accurate as the SART, is 5000 times faster, allowing for real-time image reconstruction and fluidized-bed monitoring.

By increasing the number of source-detector pairs, the precision of the XCT measurements naturally increases. However, the cost of the equipment also quickly increases. For this reason, a new reconstruction technique was devised and presented in reference (Hu et al., 2005), to obtain XCT images with only two independent projections. The authors embedded smoothing equations to increase the accuracy and took advantage of the beam hardening phenomenon by filtering the hard and soft x-rays with a rotating filter wheel with copper, lead, and air filters. This allowed them to image a gas-oil-water three-phase system with excellent accuracy when the flow is stratified. Discrepancies, however, appear for dispersed flows (bubbles of a fluid in another fluid), and the accuracy of the results is not satisfying for concentric annuli configurations. This method could be easily applied to gas-solid fluidized beds; however, the rotating wheel imposes an upper limit to the temporal resolution, which reached 4.6 Hz in this study.

One last reconstruction technique worth mentioning is the one based on Abel's integral equation with a Tikhonov Regularization (TR) presented in Section 2.2. This was compared with the FBP method and was found to return a more precise voidage distribution (Wu et al., 2008). Although in this study it was applied to a bubble column, comparable results are expected on a fluidized bed.

It is worth noting that there are two options when cone-beam 3D time-averaged XCT is implemented. Either the object image is

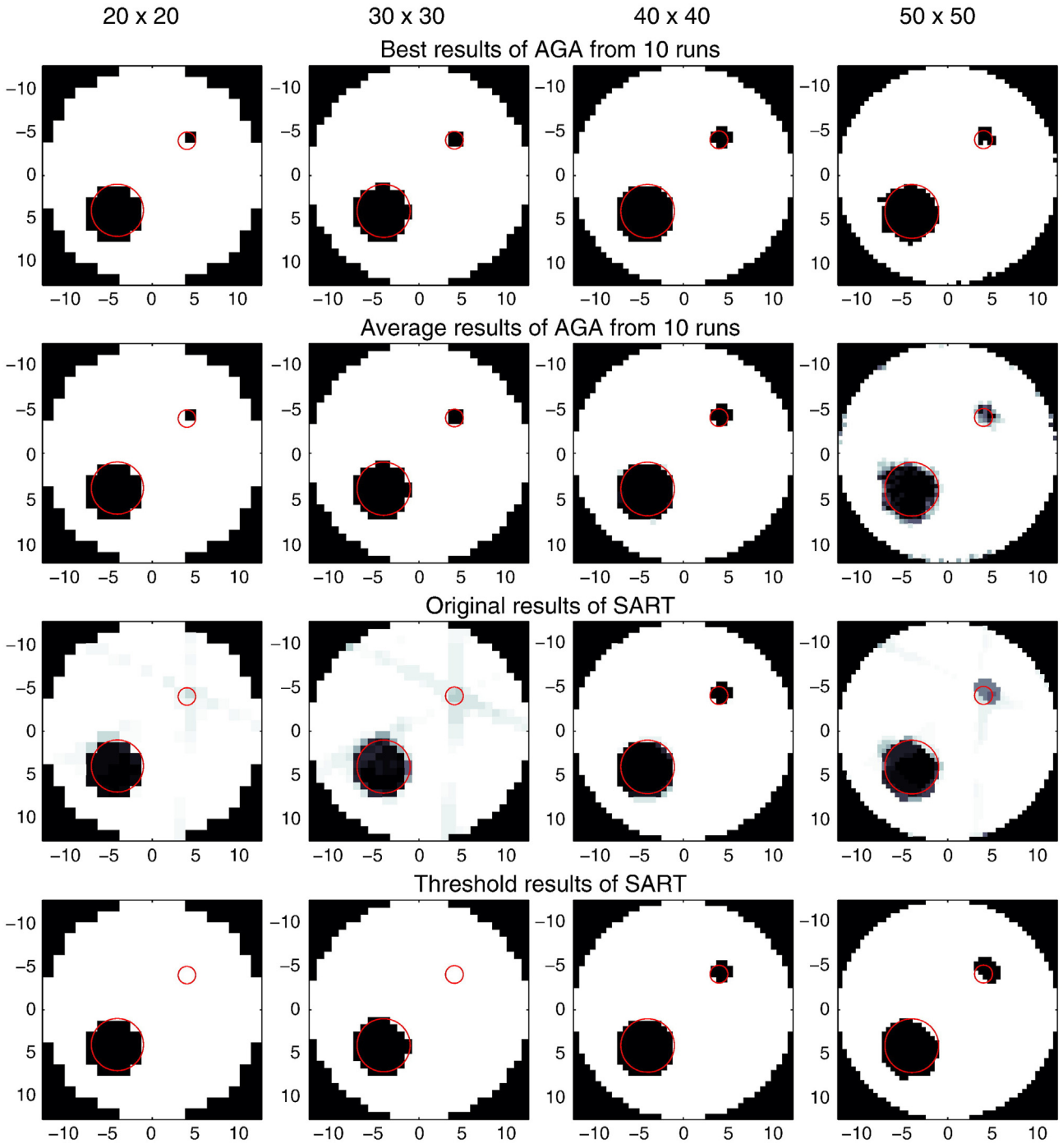

Fig. 16. Comparison between AGA image reconstruction algorithm used in reference (Yang et al., 2014b) and SART algorithm. Synthetic XCT data of a bubbling fluidized bed from three projection angles was used as input for the image reconstruction algorithms. The XCT design taken as a reference is the one with multiple sources and multiple detectors (Fig. 12(b)). The simulated vessel has a 23 cm diameter and contains two phantoms. Each column shows the reconstructed image for different image resolutions. The influence of noise on the reconstructed image quality was also studied in this work. Image reproduced with permission from reference (Yang et al., 2014b).

reconstructed row by row and then the different slices are stacked on top of each other, or a cone-beam reconstruction algorithm is used to compensate for the distortion of the projections (Heindel, 2011). The algorithm proposed by reference (Feldkamp et al., 1984) was adopted in reference (Boden et al., 2008), and the authors were able to reconstruct a time-averaged 3D image of a stirred chemical reactor with an accuracy greater than 96.5% and a voxel size of 200 μm.

3.2.3. *Normalization and calibration*

Following the image reconstruction, two other pre-processing steps are necessary: normalization and calibration. Normalization enables the comparison of consecutive frames by taking the column wall and the air around it as references that do not change during the experiment. By using the corresponding pixel values to rescale the reconstructed image, consistency across different frames can be guaranteed. Calibration, on the other hand, relies on

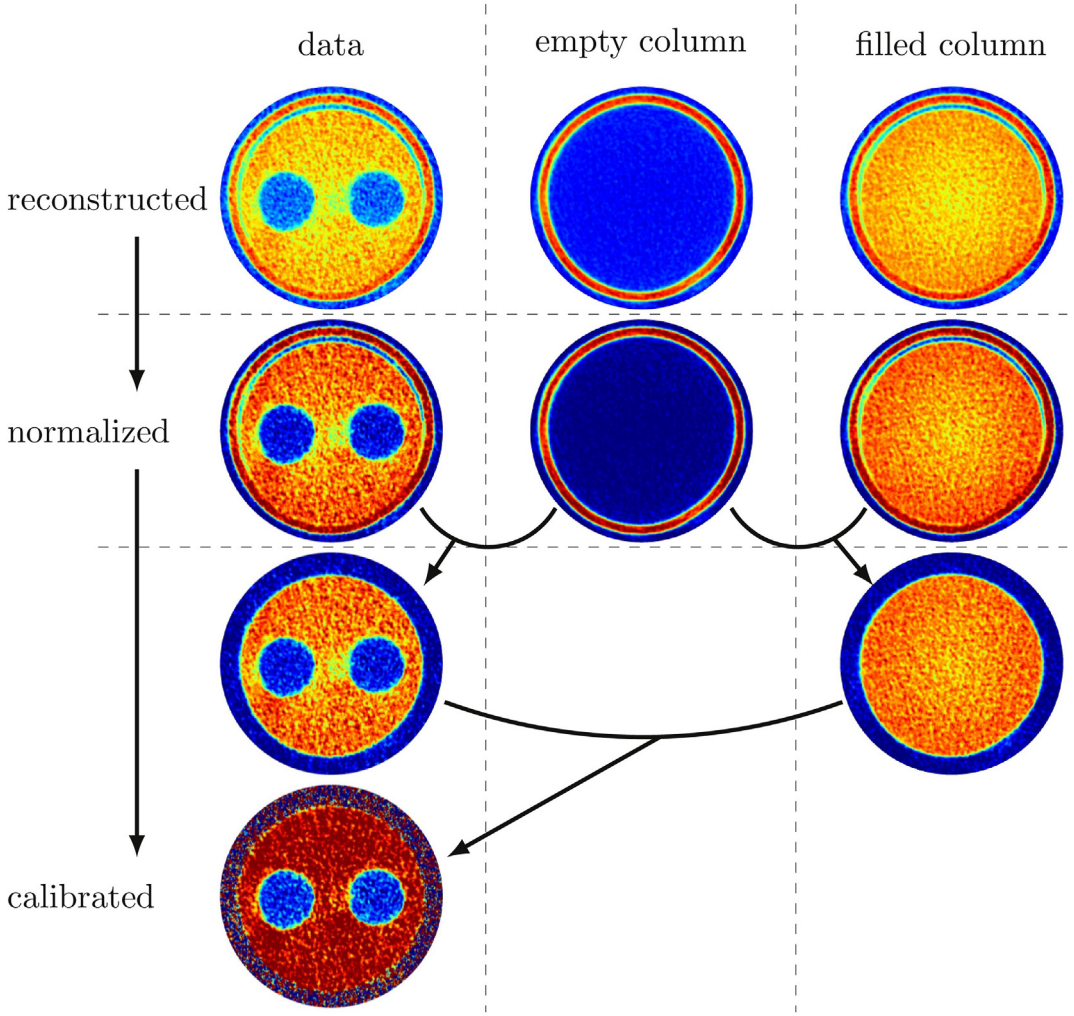

Fig. 17. Some of the pre-processing steps of XCT images, normalization and calibration, performed on a vessel with two phantoms. The normalization step, referred to the bed wall and to the air around it, is first applied to guarantee consistency between different frames. Following this, calibration with respect to the empty column and to the filled column is performed to obtain a voidage map. Image reproduced with permission from reference (Lau et al., 2018).

the reconstructed images of the empty and filled column to rescale the frame under study to a situation included between these two extremes (Lau et al., 2018). If the x-ray source settings were to be varied, the calibration step can help in minimizing the corresponding error (Morgan & Heindel, 2017). These two pre-processing methodologies are illustrated in Fig. 17.

Once the normalized and calibrated image has been obtained, smoothing is performed in order to reduce noise, and then the same post-processing steps presented for XDR in Section 2.2 can be applied.

3.3. Fluidized beds characterization

3.3.1. Voidage distribution

The direct output of XCT is an attenuation map, which can be easily converted into a voidage distribution. This can be in the form of time-averaged 2D (Grassler & Wirth, 2000) or time-averaged 3D (Deza, Franka, et al., 2009; Min et al., 2008) distributions. These experiments and simulations were performed on bubbling and circulating fluidized-bed reactors. The voidage distribution enables the study of macro structures in fluidized beds, such as bubbles and jets, as well as the validation of CFD models. A study investigated the effect of bed height and bed material density on the voidage by means of 2D horizontal and vertical slices obtained through time-averaged XCT (Escudero & Heindel, 2011). Some examples of the resulting XCT images are shown in Fig. 18. These were obtained with a rotating cone-beam and 2D-detector XCT setup, such as the one in Fig. 12(c). The same research group then obtained a time-averaged 3D voidage distribution and averaged it in the azimuthal direction, to obtain a 2D voidage map highlighting four different hydrodynamic structures occurring in the fluidized bed (Drake & Heindel, 2012). Voidage distributions in horizontal and vertical planes and voidage profiles in such planes were obtained with the same experimental setup to prove that an acoustic field can make the jets more stable and the voidage distribution more homogeneous (Escudero & Heindel, 2014a). XCT has also been used to assess the effect of local and intrusive optical probes on the local voidage (Dubrawski et al., 2013), similar to the method of reference (Tebianian et al., 2015), but with XCT. They found that these local probes, with diameters ranging from 3 mm to 4 mm, introduce an error on the average voidage that is less than 9% in dense fluidized beds. The effect of the intrusive probes was also quantified in another XCT study (Whitemarsh et al., 2016). Their results showed that, in order to minimize the effect, the probe would have to be placed in the central part of the bed, far from the distributor or in the top region of the bed, with a vertical orientation, and with the reactor operating at large fluidization velocities.

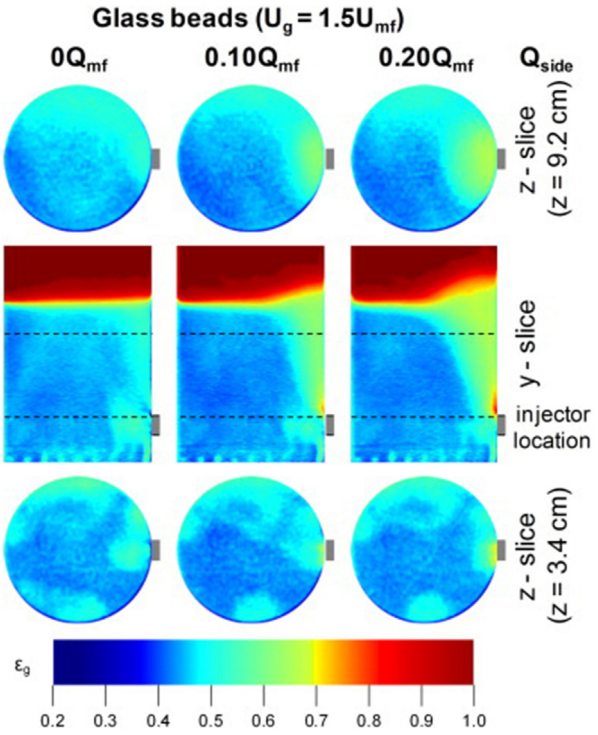

Fig. 18. Voidage distribution obtained via XCT in 2D vertical and horizontal slices of a cylindrical gas-solid fluidized bed of glass beads fluidized with air at $1.5U_{mf}$ and with lateral air injection for different injection flow rates. The fluidized bed vessel is made of PMMA and nylon. Different bed materials were tested, but the results shown here refer to glass beads. In addition to the air injected in the bed via the distributor plate, side injection is performed to reproduce the devolatilization of biomass. This XCT analysis has been performed with a rotating 2D-detector setup, such as the one in Fig. 12(c). Image reproduced with permission from reference (Franka & Heindel, 2009).

3.3.2. Bubble properties

Similar to XDR, XCT has been widely employed to characterize bubble properties. A system to study the 3D shape of bubbles using XCT coupled with image-processing techniques was presented in reference (Kai et al., 2008). The x-ray system used allowed the authors to take time-resolved images of one cross-sectional plane and, by putting together consecutive images, pseudo-3D images of bubbles could be reconstructed. This allowed the observation of the complicated and non-spherical shape of bubbles in a fluidized catalyst bed, and of their structure that appeared to be composed of multiple smaller bubbles. This particular study was able to describe the bubble shape to a level of detail of a few millimeters. The authors used these results to evaluate a corrected volume fraction of the effective catalyst layer (Kai et al., 2007). The results in references (Mudde, 2010a; Mudde, 2010b), however, do not fully agree and show more traditional bubble shapes with void and wake regions, as also shown in reference (Iannello et al., 2023). Bubbles with equivalent diameters down to 3.5 cm in a 23-cm ID fluidized bed have been observed (Mudde, 2011). The research group led by Mudde and van Ommen at the University of Technology has been the main contributor to the study of bubbles via XCT. Their system relied on three pairs of x-ray sources and 1D detector arrays, where each detector array was made up of 32 detectors. By doubling the number of detectors and placing them onto two parallel planes (Mudde, 2010b), they were able to image two parallel horizontal slices of the fluidized bed. By then comparing the reconstructed images onto the two planes, they could extract information about bubble rise velocity, size, and shape. The same imaging system was used to obtain correlations for the bubble size and velocity distribution in a fluidized bed with internals (Maurer et al., 2016a) and to analyze the effect of cohesive forces on bubble coalescence (Ma et al., 2019). The results showed that bubble coalescence is promoted by cohesive forces. The same research group studied the effect of internals on bubble properties, showing smaller and more uniform bubbles in the presence of vertical internals (Maurer et al., 2015a; Schillinger et al., 2017). Fig. 19 shows the aspect of the bubbles reconstructed with this technique. Another study focused on the difference between bubbles and slugs, with particular attention to the effect of a change in the inter-particle forces (Ma et al., 2021). XCT has also proven helpful to evaluate the bubble size and to assess the role that an increase in pressure and in fines concentration can play in improving the contact between gas and solids in a bed of group B particles by reducing the bubble size (Brouwer et al., 2012).

Also Bieberle et al. (Verma et al., 2014; Bieberle et al., 2010b), Kantzas' (Brouwer et al., 2012; Wu, Yu, et al., 2007) and Heindel's (Franka & Heindel, 2009; Drake & Heindel, 2012) research groups brought significant contributions to the knowledge of bubble properties using XCT. The first group of researchers focused on the effects of the bed material, fluidization velocity and bed height on bubble size, rise velocity and the voidage probability distribution. Kantzas' group, by contrast, studied the impact of the fluidized-bed column scale-up and of the operating conditions on the bubble properties. The group led by Heindel at Iowa State University also investigated different bed materials, fluidization velocities and column sizes, but introducing a side air injection simulating the devolatilization of biomass feedstock in a fluidized-bed gasifier and analyzing the bubble behavior. It is worth mentioning that the x-ray system at Iowa State University is capable of performing XDR, x-ray stereographic particle tracking and XCT (Escudero & Heindel, 2014a).

3.3.3. Jets

XCT has demonstrated its capabilities in the study of the other main macrostructures in gas-solid fluidized beds: jets. It enabled the 3D reconstruction through XCT of vertical jets from the distributor plate in a 3D fluidized bed of group B particles (Escudero & Heindel, 2016). These were then used to investigate the effect of acoustic vibration on the fluidization quality. They showed that acoustic vibration can increase the jet penetration length and expansion angle, for larger bed materials decrease the number of active jets, and, overall, improve the fluidization uniformity. However, this might be partially due to the lower minimum fluidization velocity under acoustic vibration acting as a confounder (Escudero & Heindel, 2013). XCT has also been used, together with other techniques, to observe the jet structure and to study the entrainment area around it (Koeninger et al., 2017). In a further study, they obtained two correlations, for the axial and radial solid concentrations in a jet (Koeninger, Koegl, Hensler, Arlt, & Wirth, 2018). Furthermore, the effect of a downward micro-nozzle as a secondary gas injection in a fluidized bed of fine particles was also investigated in reference (Yang et al., 2014a). In this last study, XCT allowed the visualization of patterns forming below the nozzle. A bubbling area, a diluted one, and a compact area were observed. The penetration length was estimated, as the jet was not directly observed. This was attributed to a limited thickness, to which the XCT system was not sensitive. The resulting penetration lengths agreed well with literature values.

3.3.4. Other quantities

Beyond the main quantities described so far, XCT has also occasionally been employed in the quantification of mass transfer properties in turbulent fluidized beds (Saayman & Nicol, 2015), to measure the velocities of tracer particles in fluidized beds (Bieberle & Barthel, 2016), and to study gas-liquid-solid

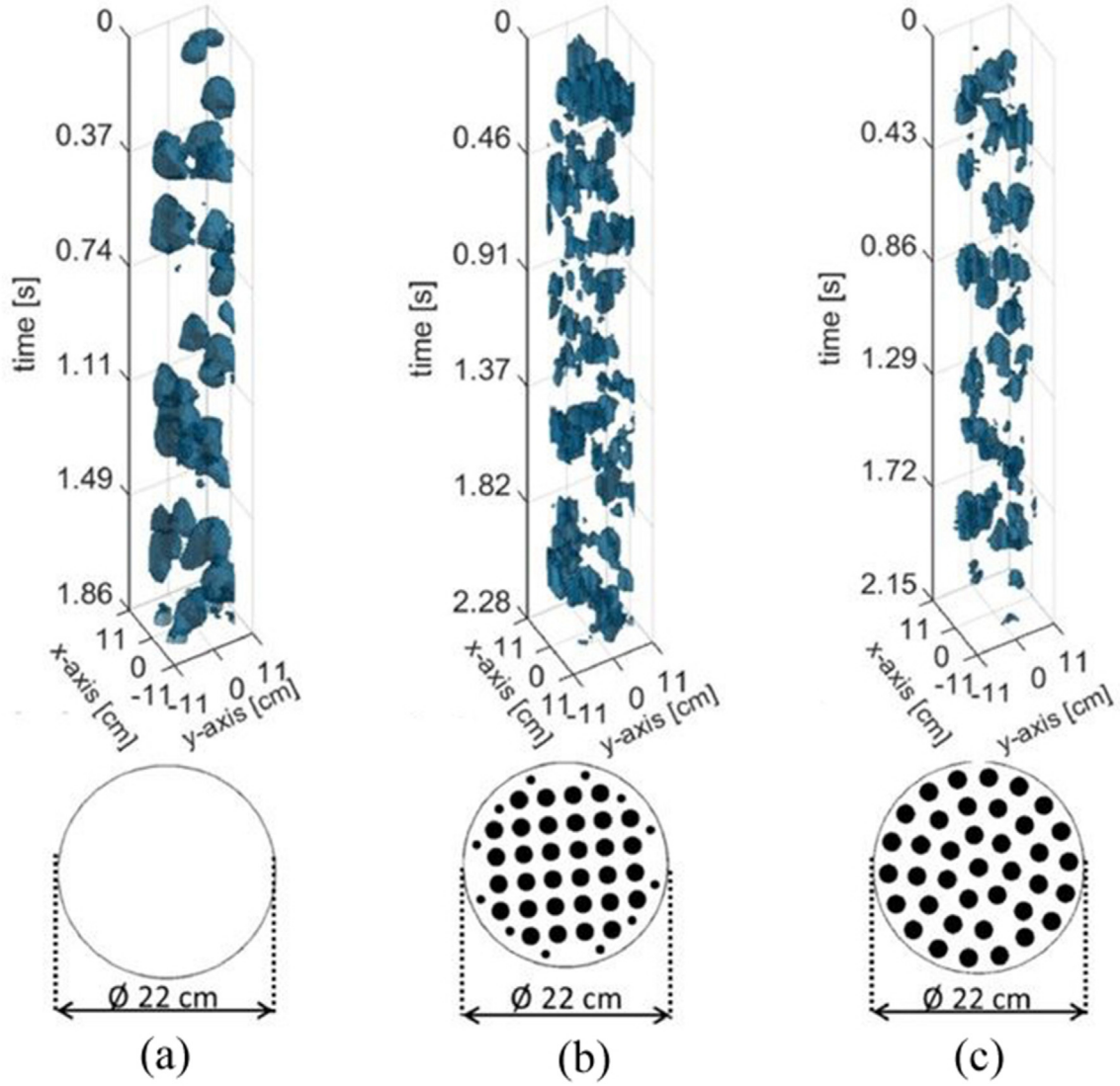

Fig. 19. Bubble reconstruction from XCT measurements in a 23-cm PMMA fluidized bed vessel with alumina particles fluidized with air at $3U_{mf}$. Three cases were studied: (a) without internals, (b) with internals with squared arrangement, (c) with internals with circular arrangements. This analysis was performed with a multiple-source multiple-detector fan-beam configuration, such as the one in Fig. 12(b). Image reproduced with permission from reference (Schillinger et al., 2017).

fluidized beds (Gehrke & Wirth, 2005). A dual energy XCT system allowed the authors of the last study to differentiate between the solid and liquid phases. A potential application of this technique is to the investigation of sprays in gas-solid fluidized beds, although, to the authors' best knowledge, this has not been done yet.

3.4. Comparison with other techniques and models

Cross-validation between XCT and other diagnostic techniques has been performed in multiple studies. For example, the time-averaged voidage radial profile at different heights, as well as the time-averaged axial voidage profile, were measured in a fluidized bed by means of optical fiber probes, dynamic pressure measurements, ECT, RPT, and XCT (Dubrawski et al., 2013). XCT was found to agree well with the other diagnostic techniques, considering that the optical fiber probes slightly overestimated the voidage. This link was then further investigated by reference (Schillinger et al., 2018), who tried to assess the overlap in bubble properties measured with the two techniques. However, they noticed differences in the bubble size and the bubble rise velocity, highlighting the need to correctly consider the statistical effect of the optical probe measurements. They proposed a correction factor that allows calculation of the mean volume equivalent diameter from the mean chord length assuming an ideal ellipsoidal geometry for the bubbles. This study aimed to validate the optical probe measurements against XCT, as the latter cannot be implemented in high-temperature applications. Finally, a further study validated some PIV and capacitance probe measurements of the solids concentration in the proximity of a jet with XCT (Koeninger et al., 2017). The good agreement between the capacitance probes and XCT seems promising for the application of capacitance probes to industrial systems, where XCT would not perform well. Measurements of the time-averaged voidage distribution via XCT were shown to exhibit a high degree of repeatability (Drake & Heindel, 2011; Drake & Heindel, 2009). They also highlighted how bed material consistency and larger superficial gas velocities contribute to a higher degree of repeatability.

As the main quantities XCT can provide are the voidage distribution and the bubble and jet properties, it has mostly been used to validate Eulerian–Eulerian two-fluid models (TFM). Other than visually, the main quantities used for validation have been time-averaged voidage profiles (Deza, Battaglia, & Heindel, 2009; Deza et al., 2011; Min et al., 2010), particle segregation number (Bai et al., 2013), bubble size and velocity (Verma et al., 2014), and jet penetration length (Panariello et al., 2022). Combining XCT, XDR, pressure response analysis, and radioactive particle tracking (RPT) can provide an excellent tool for the validation of CFD models, as shown in reference (Kantzas et al., 2001). The authors of this last work used XCT to characterize the voidage distribution in horizontal slices of the fluidized bed under study. Eulerian–Eulerian CFD simulations of a fluidized bed of glass beads, both with and without side air injection, were validated by means of time-averaged voidage distributions along vertical slices obtained via XCT (Deza, Battaglia, & Heindel, 2009; Min et al., 2010). They then used the validated model and experiments on a fluidized bed of biomass to find that the Gidaspow model is the one that better describes fluidized biomass. They also observed that the particle sphericity played a significant role in the fluidization characteristics, while the coefficient of restitution did not seem to have an effect. The same research group then validated the CFD simulations of a biomass fluidized bed with air injection through first one, and then two, side ports with the 2D vertical and horizontal voidage distribution data obtained via XCT (Deza et al., 2011). The validated model was then used to investigate the effects of the gas superficial velocity and of the side air injection flow rate on the fluidization quality (Deza & Battaglia, 2015). A comparison between XCT bubble size and velocity both with literature correlations and with two-fluid model (TFM) 3D CFD simulations for different bed materials was performed in reference (Verma et al., 2014). They noticed that small bubbles, when close to larger ones, were not observed through XCT as individual bubbles, but were instead merged with the neighboring large ones. However, the small bubbles of the same sizes were detected when isolated. This led the authors of the study to attribute the missed detection to image processing methodologies rather than to the experimental apparatus itself. Following this rationale, the smallest detectable bubble size is not expected to be an absolute value, but rather a value relative to the size of the neighboring large bubbles. These results also highlight the importance of choosing the image reconstruction algorithm and processing parameters for the steps presented in Section 3.2 that are the most suitable for the application at hand. Some further work (Panariello et al., 2022) aimed to simulate through a CFD simulation the effect of a single nozzle with two horizontal orifices and used x-ray imaging data as a validation tool. By rotating the fluidized bed, they managed to reconstruct tomographic images of the voidage distribution in the fluidized bed. Fig. 20 shows the comparison between experimental and simulation results in the description of jets in this last study.

3.5. Applications

As for XRD, XCT has been extremely useful in addressing some of the operational problems in fluidized beds, understanding them, and helping find solutions to prevent them from happening, or at least to minimize their impact. Among others, the group led by Heindel worked in this direction using XCT to study the behavior of endogenous bubbles that are created when highly volatile material, such as waste biomass, enters a fluidized-bed reactor. They reproduced the devolatilization of fuel, such as coal and biomass, by means of a side-air injection (Franka & Heindel, 2009; Drake & Heindel, 2012). The voidage distribution both in vertical and horizontal slices for different injection flow rates can be observed in Fig. 18. Although one may argue that the air injection might not be perfectly representative of the release of air by a fuel particle (Iannello et al., 2023), they mostly focused on the effect of

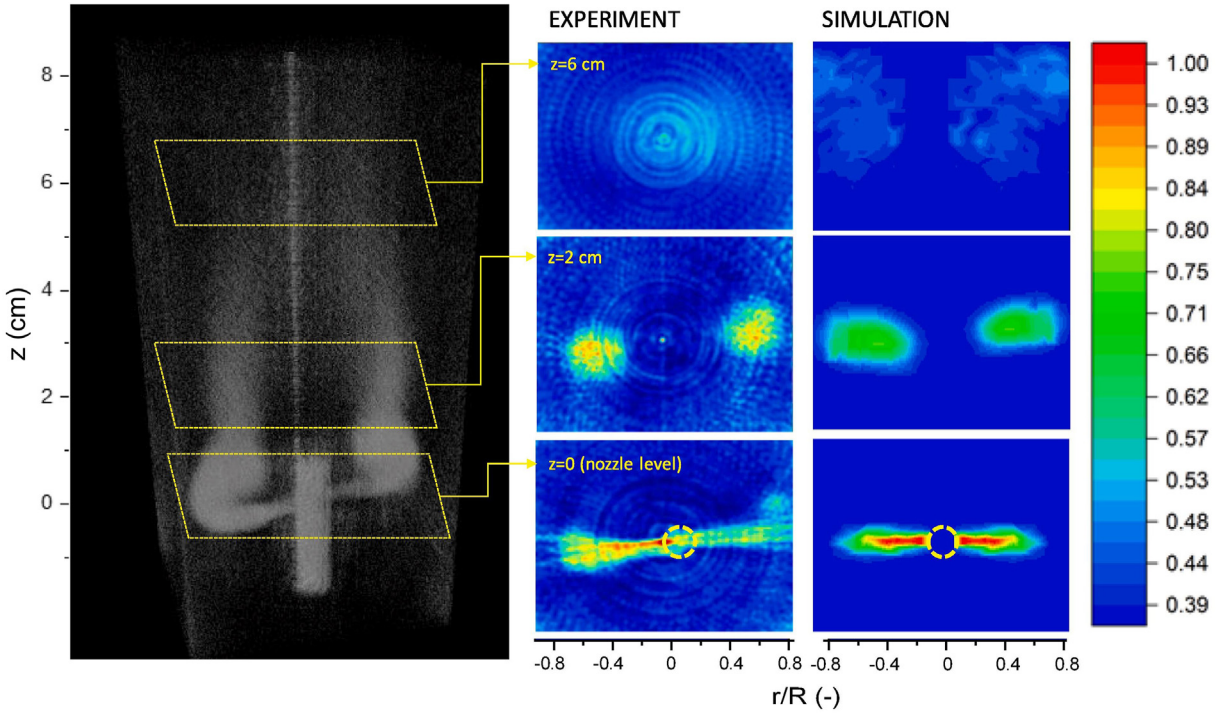

Fig. 20. Comparison between simulation and experimental results of the voidage distribution in the vicinity of a two-orifice horizontal nozzle in a fluidized bed of silica sand fluidized with air with Q_{jet}~1.2Q_{mf}. On the left, a 3D visualization is shown, while, on the right, horizontal slices at different heights are reported. The fluidized bed used for this study has a square cross section with a side of 130 mm. The bed material used is sand and it is fluidized with air. The XCT setup is a rotating one with a cone-beam and a 2D detector (Fig. 12(c)). In this case, the reactor was rotated, and the x-ray system kept still. Image reproduced with permission from reference (Panariello et al., 2022).

additional injection of air into a fluidized bed in terms of local and global time-averaged voidage. A following study from the same group then used similar experiments to validate the corresponding CFD simulations (Deza, Battaglia, & Heindel, 2009). In addition, they also validated two-fluid simulations of the mixing behavior of biomass in a fluidized bed (Bai et al., 2013). However, their analysis was performed in a cold-flow model and does not account for the volatiles that are released by biomass in high-temperature fluidized-bed reactors.

Among other applications, XCT has been used to study the effect of internals (Maurer et al., 2015a; Schillinger et al., 2017; Maurer, Wagner, et al., 2015) and of the shape of the bed material (Mema et al., 2020), as well as the scale-up effects (Wu, Yu, et al., 2007), on bubble properties. Other XCT studies, on the other hand, focused on circulating fluidized beds (Hensler et al., 2016), mass transfer in turbulent fluidized beds (Saayman & Nicol, 2015), bubble columns (Nedeltchev et al., 2017), and gas-liquid-solid fluidized beds (Gehrke & Wirth, 2005). In this latter study, specifically, the authors made use of dual-energy x-ray tomography, which allows the study of three-phase systems. This technique relies on the fact that the x-ray attenuation coefficient depends both on the medium and on the energy of the x-rays. This technique shows some promise to study, for example, sprays in gas-solid fluidized beds, however, to the authors' best knowledge, it has not yet been applied to this field.

Similar to Table 1 for XDR, Table 2 reports the main researchers studying gas-solid fluidized beds in recent years together with their XCT experimental setup and primary topics of focus.

4. Further discussion

X-ray digital radiography presents an array of advantages. Among these, is the fact that x-rays constitute a hard field, which means that they travel along straight lines and are not affected by the properties of the materials outside their direction of travel. This guarantees a simpler data processing. By contrast, soft-field measurement techniques, such as electrical capacitance tomography, need to take into account that the signal will be affected also by changes in the properties in regions outside the line of sight. XDR proved to be an excellent technique for the description of the bubble evolution along the vertical direction as it enables the capture of the whole bed height at each instant in time. Moreover, x-rays are not affected by electrostatic charge, which can easily build up in gas-solid fluidized beds. By contrast, electrical capacitance tomography is very sensitive to electrostatic charge build-up (Heindel, 2011). Finally, among the hard-field highly penetrating measurement techniques, XDR is the safest since an x-ray source can be easily shut down, in contrast with, for example, γ rays.

On the downside, XDR presents an upper limit when it comes to the size of the system that can be imaged. Although highly penetrating, x-rays through solid media are attenuated and this attenuation cannot be neglected. Fluidized-bed columns with diameters larger than a few tens of centimeters cannot be imaged with XDR. Whilst some alternative materials can help in improving the quality of x-ray images, they also affect the fluidization quality enough for this to be non-negligible (Franka et al., 2007). Moreover, the information that XDR can provide about structures and distributions in horizontal cross-sections of a fluidized bed is limited as the resulting images are 2D projections of 3D objects, collapsing the information relative to each path onto a single pixel. Finally, XDR can still pose safety concerns, even though more limited than γ-rays techniques, as it relies on the use of ionizing radiation.

X-ray digital radiography has been historically widely employed for the investigation of fluidized beds. It can still provide useful information about these systems, being particularly suited for process understanding rather than for process monitoring. XDR has shown great potential in the study of macrostructures, such as bubbles and jets, and of the effect of operating conditions on the fluidization properties. On the other hand, the limited thickness that they can penetrate and the safety concerns prevented it from being employed as a diagnostic technique for process monitoring.

As it is based on the same physical principle, many of the advantages and disadvantages of XDR also apply to x-ray computed tomography. The hard field simplifies the data processing and returns a better spatial resolution than soft field techniques such as electrical capacitance tomography, the x-ray source can easily be turned off, and it is not influenced by the presence of electrostatic charges. However, XCT does present some further advantages with respect to XDR. The most evident one is the capability of imaging the voidage distribution in a slice, or in the whole volume when time-averaged, while XDR projects as a 3D object onto a 2D plane, losing information along the third dimension. On the other hand, just like for XDR, the size of the reactors that can be imaged is limited and the image processing is computationally costly (Heindel, 2011). To overcome the first of these two issues, Franka et al., 2007 investigated alternative bed materials, such as ground walnut shell and melamine plastic. Although using these makes XCT imaging of larger fluidized beds possible, the fluidization quality with these alternative materials was found to be worse than with more commonly used glass beads. Most importantly, these alternative bed materials are not suitable for the operating conditions of industrial fluidized beds. Regarding the computational cost, optimized data processing was shown to reduce the reconstruction cost by a factor as high as 65 allowing for the reconstruction of 137 slices per second (Bieberle et al., 2017). Optimized algorithms and increased computational power will likely be the main drivers of the development of XCT in the near future. Furthermore, 3D time-resolved XCT has been proven to be feasible (Stürzel et al., 2011). However, it was only applied to a relatively small object and, with larger volumes to image, the computational cost of image processing can quickly become prohibitive. The scaling of the computational cost with the observed object size strongly depends on the image reconstruction algorithm being used and on the spatial resolution needed. A comparison between the computational cost of reconstructing images with the AGA algorithm presented in reference (Yang et al., 2014b) and the SART algorithm for different mesh sizes has been performed (Yang et al., 2014b). The trend of the computational time with respect to the mesh size appears to be approximately quadratic for the AGA algorithm and linear for the SART one. However, these trends are likely also affected by the number of projections and number of detectors forming each array, which were not varied in this study. By contrast, Wu et al. (2007) found that the computational cost of their genetic algorithm, relying on multiple populations in parallel, scales linearly with the mesh size (Wu, Cheng, et al., 2007). In addition, Gómez-Hernández et al. proposed the novel MIRR image reconstruction algorithm, capable of reducing the computational cost with respect to the SART algorithm by a factor or approximately 5000 (Gómez-Hernández et al., 2016). However, not many systematic studies comparing the computational performances, as well as the accuracy, of different image reconstruction algorithms have been performed.

On the downside, time-resolved fan-beam XCT only allows visualization of a horizontal slice of a fluidized-bed reactor, while the XDR returns images across the whole height of the fluid bed. This latter can be more useful when studying structures that develop along the fluidized bed height, such as bubbles and jets. On top of this, as the spatial resolution improves, the computational cost increases, and a balance must be found. However, this will depend on a whole variety of factors, such as the computational power available, the size of the object being imaged and the

spatial resolution required. Furthermore, there is still room for improvement in terms of robustness to noise. Finally, XCT has historically been characterized by a lower limit on the temporal resolution, reducing the capabilities of describing fast phenomena such as multiphase flows (van Ommen & Mudde, 2008; Kantzas, 2022). However, this issue has been overcome through the design of new XCT systems over the last 15 years relying on the electronic deflection of the electron beam (Bieberle, Fischer, et al., 2010). As mentioned previously, due to the nature of the XCT results, this technique is not the best option for studying vertical structures or phenomena in fluidized beds, such as bubbles and jets.

Overall, XCT has proven to be an invaluable technique to study fluidized-bed hydrodynamics. Due to the limits in size of the fluidized beds to which it can be applied and to the safety concerns related to ionizing radiation, XCT is better suited for process understanding than for process monitoring. Nevertheless, when combined with CFD simulations and other diagnostic techniques, such as optical and capacitance probes or pressure measurements, it can provide extremely useful information to better understand and master the difficult scale-up of such systems.

5. Conclusions

This work offers an overview of the x-ray imaging techniques that have most commonly been applied to fluidized beds: x-ray digital radiography and x-ray computed tomography. The main advantage of these diagnostic techniques with respect to some others is that they allow the visualization of the bed behavior without affecting the bed hydrodynamics. Each of the techniques has been described in terms of operating principles, image processing, fluidized bed quantities that can be measured, cross-validation with other techniques, and CFD validation. Furthermore, it was presented how these have been used to study some modern applications of gas-solid fluidized beds, such as waste treatment and thermochemical conversion of biomass. Both techniques are more useful for process understanding rather than for process monitoring, due to the limited size of the systems they can image and to the safety concerns related to ionizing radiation. Due to their Eulerian approach, the two imaging techniques were found to be better suited for the study of the voidage distribution and of macro structures in fluidized beds, e.g., bubbles and jets. While x-ray digital radiography enables the tracking of such structures over the bed height, x-ray computed tomography can provide a better insight when the focus is on perturbations or structures in a horizontal cross-section. Both techniques have been thoroughly cross-validated with other diagnostic techniques and have been used for the validation of CFD models. The kind of information that can be drawn with these x-ray imaging techniques is more suitable for the validation of Eulerian-Eulerian CFD simulations. Although the processing of x-ray digital radiography images consists of quite a few steps, these are relatively well established and have been employed for decades. On the other hand, image reconstruction algorithms for x-ray computed tomography have been constantly evolving and improving in the past few years. These algorithms remain the limiting factor to applying XCT in real time and significant efforts to improve them are expected in the near future.

Declaration of interest

The authors declare that they have no known competing financial interests or personal relationships that could have appeared to influence the work reported in this paper.

References

Abanades, J. C., Anthony, E. J., Lu, D. Y., Salvador, C., & Alvarez, D. (2004). Capture of CO2 from combustion gases in a fluidized bed of CaO. *AIChE Journal, 50*(7), 1614–1622. https://doi.org/10.1002/aic.10132

Abdul Wahab, Y., Abdul Rahim, R., Fazalul Rahiman, M. H., Ridzuan Aw, S., Mohd, Yunus, Goh, C. L., Abdul Rahim, H., & Ling, L. P. (2015). Non-invasive process tomography in chemical mixtures – a review Sensors and Actuators. *B: Chemical, 210*, 602–617. https://doi.org/10.1016/j.snb.2014.12.103

Ariyapadi, S., Berruti, F., Briens, C., McMillan, J., & Zhou, D. (2004). Horizontal penetration of gas-liquid spray jets in gas-solid fluidized beds. *International Journal of Chemical Reactor Engineering, 2*(1). https://doi.org/10.2202/1542-6580.1148

Ariyapadi, S., Holdsworth, D. W., Norley, C. J. D., Berruti, F., & Briens, C. (2003). Digital X-ray imaging technique to study the horizontal injection of gas-liquid jets into fluidized beds. *International Journal of Chemical Reactor Engineering, 1*(1). https://doi.org/10.2202/1542-6580.1114

Bai, W., Keller, N. K. G., Heindel, T. J., & Fox, R. O. (2013). Numerical study of mixing and segregation in a biomass fluidized bed. *Powder Technology, 237*, 355–366. https://doi.org/10.1016/j.powtec.2012.12.018

Behling, M., Mewes, D., & Dual-Energy X-Ray Tomographic Measurement of Local Phase Fractions in 3-Phase Bubble Columns. (2006). In *Proc. ASME fluids eng. Div. Summer meet. 2006, FEDSM2006, 1* pp. 1799–1806). SYPMOSIA. https://doi.org/10.1115/FEDSM2006-98142.

Belchamber, R. M. (1995). Non-invasive techniques. In *Process analytical chemistry* (pp. 329–352). Dordrecht: Springer Netherlands.

Bieberle, M., & Barthel, F. (2016). Combined phase distribution and particle velocity measurement in spout fluidized beds by ultrafast X-ray computed tomography. *Chemical Engineering Journal, 285*, 218–227. https://doi.org/10.1016/j.cej.2015.10.003

Bieberle, M., Barthel, F., & Hampel, U. (2012). Ultrafast X-ray computed tomography for the analysis of gas-solid fluidized beds. *Chemical Engineering Journal, 189*(190), 356–363. https://doi.org/10.1016/j.cej.2012.02.028

Bieberle, A., Frust, T., Wagner, M., Bieberle, M., & Hampel, U. (2017). Data processing performance analysis for ultrafast electron beam X-ray CT using parallel processing hardware architectures. *Flow Measurement and Instrumentation, 53*, 180–188. https://doi.org/10.1016/j.flowmeasinst.2016.04.004

Bieberle, M., Schleicher, E., Fischer, F., Koch, D., Menz, H.-J., Mayer, H.-G., Hampel, U., et al. (2010b). Dual-plane ultrafast limited-angle electron beam x-ray tomography. *Flow Measurement and Instrumentation, 21*(3), 233–239. https://doi.org/10.1016/j.flowmeasinst.2009.12.001

Bieberle, M., Fischer, F., Schleicher, E., Hampel, U., Koch, D., Aktay, K. S. D. C., … Mayer, H. G. (2007). Ultrafast limited-angle-type x-ray tomography. *Applied Physics Letters, 91*(12). https://doi.org/10.1063/1.2787879

Bieberle, M., Fischer, F., Schleicher, E., Menz, H. J., Mayer, H. G., & Hampel, U. (2010). Ultrafast cross-sectional imaging of gas-particle flow in a fluidized bed. *AIChE Journal, 56*(8), 2221–2225. https://doi.org/10.1002/AIC.12121

Boden, S., Bieberle, M., & Hampel, U. (2008). Quantitative measurement of gas hold-up distribution in a stirred chemical reactor using X-ray cone-beam computed tomography. *Chemical Engineering Journal, 139*(2), 351–362. https://doi.org/10.1016/j.cej.2007.08.014

Brouwer, G. C., Wagner, E. C., van Ommen, J. R., & Mudde, R. F. (2012). Effects of pressure and fines content on bubble diameter in a fluidized bed studied using fast X-ray tomography. *Chemical Engineering Journal, 207*(208), 711–717. https://doi.org/10.1016/j.cej.2012.07.040

Bruni, G., Solimene, R., Marzocchella, A., Salatino, P., Yates, J. G., Lettieri, P., & Fiorentino, M. (2002). Self-segregation of high-volatile fuel particles during devolatilization in a fluidized bed reactor. *Powder Technology, 128*(1), 11–21. https://doi.org/10.1016/S0032-5910(02)00149-3

Cao, C., & Weinstein, H. (2000). Characterization of downflowing high velocity fluidized beds. *AIChE Journal, 46*(3), 515–522. https://doi.org/10.1002/aic.690460310

Chandrasekaran, B. K., van der Lee, L., Hulme, I., & Kantzas, A. (2005). A simulation and experimental study of the hydrodynamics of a bubbling fluidized bed of linear low density polyethylene using bubble properties and pressure fluctuations. *Macromolecular Materials and Engineering, 290*(6), 592–609. https://doi.org/10.1002/mame.200500065

Chaouki, J., Larachi, F., & Dudukovic, M. P. (1997). Non-invasive monitoring of multiphase flows. *Non-invasive Monit. Multiph. flows*. https://doi.org/10.1016/B978-0-444-82521-6.X5000-1

Chaplin, G., Pugsley, T., Van Der Lee, L., Kantzas, A., & Winters, C. (2005). The dynamic calibration of an electrical capacitance tomography sensor applied to the fluidized bed drying of pharmaceutical granule. *Measurement Science and Technology, 16*(6), 1281–1290. https://doi.org/10.1088/0957-0233/16/6/007

Chen, X., Zhong, W., & Heindel, T. J. (2019a). Orientation of cylindrical particles in a fluidized bed based on stereo X-ray particle tracking velocimetry (XPTV). *Chemical Engineering Science, 203*, 104–112. https://doi.org/10.1016/j.ces.2019.03.067

Chen, X., Zhong, W., & Heindel, T. J. (2019b). Using stereo XPTV to determine cylindrical particle distribution and velocity in a binary fluidized bed. *AIChE Journal, 65*(2), 520–535. https://doi.org/10.1002/aic.16485

Deza, M., & Battaglia, F. (2015). *Effects of increasing inlet velocities and side port air injection on a biomass fluidizing bed*.

Deza, M., Battaglia, F., & Heindel, T. J. (2009). In *Modeling a biomass fluidizing bed with side port air injection* (Vol. 1, pp. 1151–1159). Symposia. https://doi.org/10.1115/FEDSM2009-78372. Parts A, B and C.

Deza, M., Franka, N. P., Heindel, T. J., & Battaglia, F. (2009). CFD modeling and X-ray imaging of biomass in a fluidized bed. *Journal of Fluids Engineering, 131*(11), 1113031–11130311. https://doi.org/10.1115/1.4000257

Deza, M., Heindel, T. J., & Battaglia, F. (2011). Effects of mixing using side port air injection on a biomass fluidized bed. *Journal of Fluids Engineering, 133*(11). https://doi.org/10.1115/1.4005136

Drake, J. B., Franka, N. P., & Heindel, T. J. (2008). X-ray particle tracking velocimetry for applications in fluidized beds. In *2008 ASME international mechanical engineering congress and exposition* (pp. 379–386). https://doi.org/10.1115/IMECE2008-66224

Drake, J. B., & Heindel, T. J. (2009). Repeatability of gas holdup in a fluidized bed using X-ray computed tomography. *Proceedings of the ASME 2009 Fluids Engineering Division Summer Meeting, 1*, 1721–1731. https://doi.org/10.1115/FEDSM2009-78041. PART C.

Drake, J. B., & Heindel, T. J. (2011). The repeatability and uniformity of 3D fluidized beds. *Powder Technology, 213*(1–3), 148–154. https://doi.org/10.1016/j.powtec.2011.07.027

Drake, J. B., & Heindel, T. J. (2012). Comparisons of annular hydrodynamic structures in 3D fluidized beds using X-ray computed tomography imaging. *Journal of Fluids Engineering, 134*(8). https://doi.org/10.1115/1.4007119

Drake, J. B., & Heindel, T. J. (2012). Local time-average gas holdup comparisons in cold flow fluidized beds with side-air injection. *Chemical Engineering Science, 68*(1), 157–165. https://doi.org/10.1016/j.ces.2011.09.023

Drake, J. B., Kenney, A. L., Morgan, T. B., & Heinde, T. J. (2011). *Developing tracer particles for X-ray particle tracking velocimetry*.

Drake, J. B., Tang, L., & Heindel, T. J. (2009). X-ray particle tracking velocimetry in fluidized beds. *Proceedings of the ASME Fluids Engineering Division Summer Conference, 1*(PART C), 1733–1742. https://doi.org/10.1115/FEDSM2009-78150, 2009, FEDSM2009.

Dubrawski, K., Tebianian, S., Bi, H. T., Chaouki, J., Ellis, N., Gerspacher, R., … Grace, J. R. (2013). Traveling column for comparison of invasive and non-invasive fluidization voidage measurement techniques. *Powder Technology, 235*, 203–220. https://doi.org/10.1016/j.powtec.2012.10.031

Errigo, M., Sebastiani, A., Iannello, S., Materazzi, M., & Lettieri, P. (2023). Application of imaging techniques for the characterization of lumps behaviour in gas – solid fluidized-bed reactors. *Fuel, 349*, 128634. https://doi.org/10.1016/j.fuel.2023.128634

Escudero, D., & Heindel, T. J. (2013). Minimum fluidization velocity in a 3D fluidized bed modified with an acoustic field. *Chemical Engineering Journal, 231*, 68–75. https://doi.org/10.1016/j.cej.2013.07.011

Escudero, D. R., & Heindel, T. J. (2014a). Acoustic fluidized bed hydrodynamics characterization using X-ray computed tomography. *Chemical Engineering Journal, 243*, 411–420. https://doi.org/10.1016/j.cej.2014.01.025

Escudero, D. R., & Heindel, T. J. (2014b). *Characterizing acoustic fluidized bed hydrodynamics using x-ray computed tomography*.

Escudero, D., & Heindel, T. J. (Aug. 2011). Bed height and material density effects on fluidized bed hydrodynamics. *Chemical Engineering Science, 66*(16), 3648–3655. https://doi.org/10.1016/j.ces.2011.04.036

Escudero, D. R., & Heindel, T. J. (2016). Characterizing jetting in an acoustic fluidized bed using X-ray computed tomography. *Journal of Fluids Engineering, 138*(4). https://doi.org/10.1115/1.4031681

Feldkamp, L. A., Davis, L. C., & Kress, J. W. (1984). Practical cone-beam algorithm. *Journal of the Optical Society of America, 1*(6), 612. https://doi.org/10.1364/JOSAA.1.000612

Fischer, F., Hoppe, D., Schleicher, E., Mattausch, G., Flaske, H., Bartel, R., & Hampel, U. (2008). An ultra fast electron beam x-ray tomography scanner. *Measurement Science and Technology, 19*(9), 094002. https://doi.org/10.1088/0957-0233/19/9/094002

Franka, N. P., & Heindel, T. J. (2009). Local time-averaged gas holdup in a fluidized bed with side air injection using X-ray computed tomography. *Powder Technology, 193*(1), 69–78. https://doi.org/10.1016/j.powtec.2009.02.008

Franka, N. P., Heindel, T. J., & Battaglia, F. (2007). Visualizing cold-flow fluidized beds with X-rays. *Proceeding of IMECE2007, 37*(1), 99–105. https://doi.org/10.1115/IMECE2007-43073

Gehrke, S., & Wirth, K.-E. (2005). Application of conventional- and dual-energy X-ray tomography in process engineering. *IEEE Sensors Journal, 5*(2), 183–187. https://doi.org/10.1109/JSEN.2005.843890

Glicksman, L. R., Hyre, M. R., & Farrell, P. A. (1994). Dynamic similarity in fluidization. *International Journal of Multiphase Flow, 20*(SUPPL. 1), 331–386. https://doi.org/10.1016/0301-9322(94)90077-9

Gómez-Hernández, J., Ruud van Ommen, J., Wagner, E., & Mudde, R. F. (2016). A fast reconstruction algorithm for time-resolved X-ray tomography in bubbling fluidized beds. *Powder Technology, 290*, 33–44. https://doi.org/10.1016/j.powtec.2015.08.038

Grassler, T., & Wirth, K.-E. (2000). X-ray computer tomography — potential and limitation for the measurement of local solids distribution in circulating fluidized beds. *Chemical Engineering Journal, 77*(1–2), 65–72. https://doi.org/10.1016/S1385-8947(99)00133-3

Grohse, E. W. (1955). Analysis of gas-fluidized solid systems by x-ray absorption. *AIChE Journal, 1*(3), 358–365. https://doi.org/10.1002/aic.690010315

Heindel, T. J. (2011). A review of X-ray flow visualization with applications to multiphase flows. *Journal of Fluids Engineering, 133*(7). https://doi.org/10.1115/1.4004367

Heindel, T. J., Gray, J. N., & Jensen, T. C. (2008). An X-ray system for visualizing fluid flows. *Flow Measurement and Instrumentation, 19*(2), 67–78. https://doi.org/10.1016/j.flowmeasinst.2007.09.003

Gundogdu, O., Jenneson, P. M., & Tuzun, U. (2007). Nano particle fluidisation in model 2-D and 3-D beds using high speed X-ray imaging and microtomography. *Journal of Nanoparticle Research, 9*(2), 215–223. https://doi.org/10.1007/s11051-006-9169-3

He, Z., Wu, B., Chandrasekaran, B., Bellehumeur, C., & Kantzas, A. (2007). X-ray fluoroscopy measurements and CFD simulation of hydrodynamics in a two dimensional gas-solids fluidized bed. In *The 12th international conference on fluidization - new horizons in fluidization engineering* (pp. 481–488) [Online]. Available: http://dc.engconfintl.org/fluidizationxii/58FLUIDIZATIONXII. (Accessed 25 March 2022).

Hensler, T., Firsching, M., Bonilla, J. S. G., Wörlein, T., Uhlmann, N., & Wirth, K.-E. (2016). Non-invasive investigation of the cross-sectional solids distribution in CFB risers by X-ray computed tomography. *Powder Technology, 297*, 247–258. https://doi.org/10.1016/j.powtec.2016.04.030

Hu, B., Stewart, C., Hale, C. P., Lawrence, C. J., Hall, A. R. W., Zwiens, H., & Hewitt, G. F. (2005). Development of an X-ray computed tomography (CT) system with sparse sources: Application to three-phase pipe flow visualization. *Experiments in Fluids, 39*(4), 667–678. https://doi.org/10.1007/s00348-005-1008-2

Hulme, I., & Kantzas, A. (2004). Determination of bubble diameter and axial velocity for a polyethylene fluidized bed using X-ray fluoroscopy. *Powder Technology, 147*(1–3), 20–33. https://doi.org/10.1016/j.powtec.2004.08.008

Hulme, I., & Kantzas, A. (2005). Validation of bubble properties of a bubbling fluidized bed reactor using CFD with imaging experiments. *Polymer - Plastics Technology and Engineering, 44*(1), 73–95. https://doi.org/10.1081/PTE-200046041

Iannello, S., Bond, Z., Sebastiani, A., Errigo, M., & Materazzi, M. (2022). Axial segregation behaviour of a reacting biomass particle in fluidized bed reactors: Experimental results and model validation. *Fuel, 338*(December 2022), 127234. https://doi.org/10.2139/ssrn.4271228

Iannello, S., Foscolo, P. U., & Materazzi, M. (2022). Investigation of single particle devolatilization in fluidized bed reactors by X-ray imaging techniques. *Chemical Engineering Journal, 431*, 133807. https://doi.org/10.1016/j.cej.2021.133807

Iannello, S., Macrì, D., & Materazzi, M. (2023). A comprehensive assessment of endogenous bubbles properties in fluidized bed reactors via X-ray imaging. *Powder Technology, 413*, 118013. https://doi.org/10.1016/j.powtec.2022.118013

Iannello, S., Morrin, S., & Materazzi, M. (2020). Fluidised bed reactors for the thermochemical conversion of biomass and waste. *KONA Powder Part. J, 37*(37), 114–131. https://doi.org/10.14356/kona.2020016

Jenneson, P. M., & Gundogdu, O. (2006). In situ x-ray imaging of nanoparticle agglomeration in fluidized beds. *Applied Physics Letters, 88*(3), 034103. https://doi.org/10.1063/1.2166486

Kai, T., Misawa, M., Takahashi, T., Tiseanu, I., & Ichikawa, N. (2008). Observation of 3-D structure of bubbles in a fluidized catalyst bed. *Canadian Journal of Chemical Engineering, 83*(1), 113–118. https://doi.org/10.1002/cjce.5450830119

Kai, T., Okada, N., Baba, M., Takahashi, T., Misawa, M., Tiseanu, I., & Ichikawa, N. (2007). Structure of effective catalyst layers around bubbles in a fluidized catalyst bed. *Chemical Engineering Journal, 130*(2–3), 119–124. https://doi.org/10.1016/j.cej.2006.06.017

Kantzas, A. (2022). *X-ray tomography of fluidized beds*. Elsevier Ltd.

Kantzas, A. (1994). Computation of holdups in fluidized and trickle beds by computer-assisted tomography. *AIChE Journal, 40*(7), 1254–1261. https://doi.org/10.1002/aic.690400716

Kantzas, A., Wright, I., Bhargava, A., Li, F., & Hamilton, K. (2001). Measurement of hydrodynamic data of gas-phase polymerization reactors using non-intrusive methods. *Catalysis Today, 64*(3–4), 189–203. https://doi.org/10.1016/S0920-5861(00)00523-X

Knowlton, T. M. (2013). Fluidized bed reactor design and scale-up. In *Fluidized bed technologies for near-zero emission combustion and gasification* (pp. 481–523). Woodhead Publishing Limited, 1962.

Koeninger, B., Hensler, T., Schug, S., Arlt, W., & Wirth, K.-E. (2017). Horizontal secondary gas injection in fluidized beds: Solid concentration and velocity in multiphase jets. *Powder Technology, 316*, 49–58. https://doi.org/10.1016/j.powtec.2017.01.057

Koeninger, B., Koegl, T., Hensler, T., Arlt, W., & Wirth, K.-E. (2018). Solid distribution in fluidized and fixed beds with horizontal high speed gas jets. *Powder Technology, 336*, 57–69. https://doi.org/10.1016/j.powtec.2018.05.035

Lau, Y. M., Hampel, U., & Schubert, M. (2018). Ultrafast X-ray tomographic imaging of multiphase flow in bubble columns - Part 1: Image processing and reconstruction comparison. *International Journal of Multiphase Flow, 104*, 258–271. https://doi.org/10.1016/j.ijmultiphaseflow.2018.02.010

Leckner, B., Szentannai, P., & Winter, F. (2011). Scale-up of fluidized-bed combustion - a review. *Fuel, 90*(10), 2951–2964. https://doi.org/10.1016/j.fuel.2011.04.038

Lettieri, P., & Macrì, D. (2016). Effect of process conditions on fluidization. *KONA Powder Part. J., 2016*(33), 86–108. https://doi.org/10.14356/kona.2016017

Lettieri, P., Newton, D., & Yates, J. (2001). High temperature effects on the dense phase properties of gas fluidized beds. *Powder Technology, 120*(1–2), 34–40. https://doi.org/10.1016/S0032-5910(01)00344-8

Lettieri, P., & Yates, J. G. (2013). New generation X-ray imaging for multiphase systems. In *The 14th international conference on fluidization – from fundamentals to products* (pp. 641–648).

Ma, J., Liu, D., Chen, X., Liang, C., & van Ommen, J. R. (2021). X-ray tomography analysis of bubbles and slugs in a fluidized bed with inter-particle force. *International Journal of Multiphase Flow, 145*, 103835. https://doi.org/10.1016/j.ijmultiphaseflow.2021.103835

Ma, J., van Ommen, Liu, D., Mudde, R. F., Chen, X., … Liang, C. (2019). Fluidization dynamics of cohesive geldart B particles. Part I: X-Ray tomography analysis. *Chemical Engineering Journal, 359*, 1024–1034. https://doi.org/10.1016/j.cej.2018.11.082

MacDonald, C. A. (2017). *An introduction to X-ray physics, optics, and applications*. Princeton University Press.

Liu, T., Malcolm, A. A., & Xu, J. (2009). Pincushion distortion correction in x-ray imaging with an image intensifier. *Fourth International Conference on Experimental Mechanics, 7522*(April 2010), 75223T. https://doi.org/10.1117/12.851232

Macrì, D., Sutcliffe, S., & Lettieri, P. (2019). Fluidized bed sintering in TiO2 and coke systems. *Chemical Engineering Journal, 381*, 2020. https://doi.org/10.1016/j.cej.2019.122711

Maranic, Z., Guillard, F., Baker, J., Einav, I., & Marks, B. (2021). A granular thermometer. *Granular Matter, 23*(2), 19. https://doi.org/10.1007/s10035-020-01081-3

Materazzi, M., Lettieri, P., Dodds, J. M., & Milliken, A. (2017). X-ray imaging for design of gas nozzles in large scale fluidised bed reactors. *Powder Technology, 316*, 41–48. https://doi.org/10.1016/j.powtec.2016.12.089

Maurer, S., Wagner, E. C., van Ommen, J. R., Schildhauer, T. J., Teske, S. L., Biollaz, S. M. A., Wokaun, A., & Mudde, R. F. (2015a). Influence of vertical internals on a bubbling fluidized bed characterized by X-ray tomography. *International Journal of Multiphase Flow, 75*, 237–249. https://doi.org/10.1016/j.ijmultiphaseflow.2015.06.001

Maurer, S., Gschwend, D., Wagner, E. C., Schildhauer, T. J., Ruud van Ommen, J., Biollaz, S. M. A., & Mudde, R. F. (2016). Correlating bubble size and velocity distribution in bubbling fluidized bed based on X-ray tomography. *Chemical Engineering Journal, 298*, 17–25. https://doi.org/10.1016/j.cej.2016.02.012

Maurer, S., Wagner, E. C., Schildhauer, T. J., van Ommen, J. R., Biollaz, S. M. A., & Mudde, R. F. (2015). X-ray measurements of bubble hold-up in fluidized beds with and without vertical internals. *International Journal of Multiphase Flow, 74*, 118–124. https://doi.org/10.1016/j.ijmultiphaseflow.2015.03.009

Mema, I., Wagner, E. C., van Ommen, J. R., & Padding, J. T. (2020). Fluidization of spherical versus elongated particles - experimental investigation using X-ray tomography. *Chemical Engineering Journal, 397*, 125203. https://doi.org/10.1016/j.cej.2020.125203

Min, J., Drake, J., Fox, R., & Heindel, T. J. (2008). CFD modeling of cold-flow fluidized beds and validation with X-ray computed tomography. In *AIChE annual meeting 2008 conference proceedings*. November.

Min, J., Drake, J. B., Heindel, T. J., & Fox, R. O. (2010). Experimental validation of CFD simulations of a lab-scale fluidized-bed reactor with and without side-gas injection. *AIChE Journal, 56*(6), 1434–1446. https://doi.org/10.1002/aic.12077

Morgan, T. B., Halls, B. R., Meyer, T. R., & Heindel, T. J. (2013). A high-speed X-ray detector system for noninvasive fluid flow measurements. In *Volume 1C, symposia: Gas-liquid two-phase flows; industrial and environmental applications of fluid mechanics; issues and perspectives in automotive flows; liquid-solids flows; multiscale methods for multiphase flow; noninvasive measurements in single and: 1 C*. https://doi.org/10.1115/FEDSM2013-16427. V01CT24A004.

Morgan, T. B., & Heindel, T. J. (2017). Sensitivity of X-ray computed tomography measurements of a gas-solid flow to variations in acquisition parameters. *Flow Measurement and Instrumentation, 55*, 82–90. https://doi.org/10.1016/j.flowmeasinst.2016.10.011

Mudde, R. F. (2010a). Time-resolved X-ray tomography of a fluidized bed. *Powder Technology, 199*(1), 55–59. https://doi.org/10.1016/j.powtec.2009.04.021

Mudde, R. F. (2010b). Double X-ray tomography of a bubbling fluidized bed. *Industrial & Engineering Chemistry Research, 49*(11), 5061–5065. https://doi.org/10.1021/ie901537z

Mudde, R. F. (2011). Bubbles in a fluidized bed: A fast X-ray scanner. *AIChE Journal, 57*(10), 2684–2690. https://doi.org/10.1002/aic

Mudde, R. F., Alles, J., & van der Hagen, T. H. J. J. (2008). Feasibility study of a time-resolving x-ray tomographic system. *Measurement Science and Technology, 19*(8), 085501. https://doi.org/10.1088/0957-0233/19/8/085501

Nedeltchev, S., Hampel, U., & Schubert, M. (2017). Extraction of information and reconstruction entropies from ultrafast X-ray tomography data in a bubble column. *Chemical Engineering Science, 170*, 225–233. https://doi.org/10.1016/j.ces.2017.03.020

Newton, D., Fiorentino, M., & Smith, G. B. (2001). The application of X-ray imaging to the developments of fluidized bed processes. *Powder Technology, 120*(1–2), 70–75. https://doi.org/10.1016/S0032-5910(01)00349-7

Orta, A., Wu, B., Ghods, M., Guerrero, A., Bellehumeur, C., & Kantzas, A. (2011). Pressure effect on hydrodynamics of a high pressure X-ray transparent polyethylene fluidized bed. *International Journal of Chemical Reactor Engineering, 9*(1). https://doi.org/10.2202/1542-6580.2722

Panariello, L., Materazzi, M., Solimene, R., Salatino, P., & Lettieri, P. (2017). X-ray imaging of horizontal jets in gas fluidised bed nozzles. *Chemical Engineering Science, 164*, 53–62. https://doi.org/10.1016/j.ces.2017.01.055

Pore, M., Ong, G. H., Boyce, C. M., Materazzi, M., Gargiuli, J., Leadbeater, T., … Parker, D. J. (2015). A comparison of magnetic resonance, X-ray and positron emission particle tracking measurements of a single jet of gas entering a bed of particles. *Chemical Engineering Science, 122*, 210–218. https://doi.org/10.1016/j.ces.2014.09.029

Romero, J. B., & Smith, D. W. (1965). Flash x-ray analysis of fluidized beds. *AIChE Journal, 11*(4), 595–600. https://doi.org/10.1002/aic.690110408

Rowe, P. N., & Partridge, B. A. (1965). An x-ray study of bubbles in fluidised beds. *Transactions of the Institution of Chemical Engineers, 43*, 116–134. https://doi.org/10.1016/S0263-8762(97)80009-3

Rowe, P. N., Santoro, L., & Yates, J. G. (1978). The division of gas between bubble and interstitial phases in fluidised beds of fine powders. *Chemical Engineering Science, 33*(1), 133–140. https://doi.org/10.1016/0009-2509(78)85079-9

Saayman, J., & Nicol, W. (2015). Interphase mass transfer of the high velocity bubbling fluidization regime. *Chemical Engineering Research and Design, 93*, 213–223. https://doi.org/10.1016/j.cherd.2014.06.023

Schillinger, F., Maurer, S., Wagner, E. C., van Ommen, J. R., Mudde, R. F., & Schildhauer, T. J. (2017). Influence of vertical heat exchanger tubes, their arrangement and the column diameter on the hydrodynamics in a gas–solid bubbling fluidized bed. *International Journal of Multiphase Flow, 97*, 46–59. https://doi.org/10.1016/j.ijmultiphaseflow.2017.07.013

Schillinger, F., Schildhauer, T. J., Maurer, S., Wagner, E., Mudde, R. F., & van Ommen, J. R. (2018). Generation and evaluation of an artificial optical signal based on X-ray measurements for bubble characterization in fluidized beds with vertical internals. *International Journal of Multiphase Flow, 107*, 16–32. https://doi.org/10.1016/j.ijmultiphaseflow.2018.03.002

Sebastiani, A., Macrì, D., Gallucci, K., & Materazzi, M. (2021). Steam - oxygen gasification of refuse derived fuel in fluidized beds: Modelling and pilot plant testing. *Fuel Processing Technology, 216*, 106783. https://doi.org/10.1016/j.fuproc.2021.106783

Stürzel, T., Bieberle, M., Laurien, E., Hampel, U., Barthel, F., Menz, H.-J., & Mayer, H.-G. (2011). Experimental facility for two- and three-dimensional ultrafast electron beam x-ray computed tomography. *Review of Scientific Instruments, 82*(2), 023702. https://doi.org/10.1063/1.3529435

Tebianian, S., Ellis, N., Lettieri, P., & Grace, J. R. (2015). X-ray imaging for flow characterization and investigation of invasive probe interference in travelling fluidized bed. *Chemical Engineering Research and Design, 104*, 191–202. https://doi.org/10.1016/j.cherd.2015.08.006

van Ommen, J. R., & Mudde, R. F. (2008). Measuring the gas-solids distribution in fluidized beds – A review. *International Journal of Chemical Reactor Engineering, 6*(1), 1–29. https://doi.org/10.2202/1542-6580.1796

Verma, V., Padding, J. T., Deen, N. G., Kuipers, J. A. M. (Hans), Barthel, F., Bieberle, M., Wagner, M. C., & Hampel, U. (2014). Bubble dynamics in a 3-D gas–solid fluidized bed using ultrafast electron beam X-ray tomography and two-fluid model. *AIChE Journal, 59*(2), 346–354. https://doi.org/10.1002/aic.14002

Whitemarsh, E. A., Escudero, D. R., & Heindel, T. J. (2016). Probe effects on the local gas holdup conditions in a fluidized bed. *Powder Technology, 294*, 191–201. https://doi.org/10.1016/j.powtec.2016.02.035

Wormsbecker, M., Pugsley, T., van Ommen, J. R., Nijenhuis, J., & Mudde, R. (2009). Effect of distributor design on the bottom zone hydrodynamics in a fluidized bed dryer using 1-D X-ray densitometry imaging. *Industrial & Engineering Chemistry Research, 48*(15), 7004–7015. https://doi.org/10.1021/ie900025n

Wright, I., Hamilton, K., Kruychkov, S., Chen, J., Li, F., & Kantzas, A. (2001). On the measurement of hydrodynamic properties of an air-polyethylene fluidized bed system. *Chemical Engineering Science, 56*(13), 4085–4097. https://doi.org/10.1016/S0009-2509(01)00079-3

Wu, C., Cheng, Y., Ding, Y., Wei, F., & Jin, Y. (2007). A novel X-ray computed tomography method for fast measurement of multiphase flow. *Chemical Engineering Science, 62*(16), 4325–4335. https://doi.org/10.1016/j.ces.2007.04.026

Wu, B., Kantzas, A., Bellehumeur, C. T., He, Z., & Kryuchkov, S. (2007). Multi-resolution analysis of pressure fluctuations in a gas-solids fluidized bed: Application to glass beads and polyethylene powder systems. *Chemical Engineering Journal, 131*(1–3), 23–33. https://doi.org/10.1016/j.cej.2006.12.001

Wu, B., Yu, G., Bellehumeur, C., & Kantzas, A. (2007). Dynamic flow behavior measurements in gas–solid fluidized beds using different non-intrusive techniques and polyethylene powder. *Flow Measurement and Instrumentation, 18*(5–6), 197–203. https://doi.org/10.1016/j.flowmeasinst.2007.06.009

Wu, C., Cheng, Y., Liu, M., & Jin, Y. (2008). Measurement of axisymmetric two-phase flows by an improved X-ray-computed tomography technique. *Industrial & Engineering Chemistry Research, 47*(6), 2063–2074. https://doi.org/10.1021/ie071002w

Yang, X., van Ommen, J. R., & Mudde, R. F. (2014a). Comparison of genetic algorithm and algebraic reconstruction for X-ray tomography in bubbling fluidized beds. *Powder Technology, 253*, 626–637. https://doi.org/10.1016/j.powtec.2013.12.007

Yang, X., van Ommen, J. R., & Mudde, R. F. (2014b). Comparison of genetic algorithm and algebraic reconstruction for X-ray tomography in bubbling fluidized beds. *Powder Technology, 253*, 626–637. https://doi.org/10.1016/j.powtec.2013.12.007

Yates, J., Cheesman, D., Lettieri, P., & Newton, D. (2002). X-ray analysis of fluidized beds and other multiphase systems. *KONA Powder Part. J., 20*(March), 133–143. https://doi.org/10.14356/kona.2002016

Yates, J. G., & Lettieri, P. (2016). *Fluidized-bed reactors: Processes and operating conditions, 26* p. 10). Cham: Springer International Publishing.

Panariello, L., Macrí, D., Zito, V., Solimene, R., Salatino, Lettieri, P., & Materazzi, M. (2022). Experimental and numerical analysis of jet penetration and gas evolution in a single-nozzle distributor fluidized bed. *Chemical Engineering Journal, 437*(P2), 135391. https://doi.org/10.1016/j.cej.2022.135391